

# Multi-year robotic observations reveal the seasonality of downward carbon export pathways in the Southern Ocean

Léo Lacour (✉ [leo.lacour@utas.edu.au](mailto:leo.lacour@utas.edu.au))

Institute for Marine and Antarctic Studies <https://orcid.org/0000-0003-1792-5969>

Joan Lloret

Barcelona Supercomputing Centre <https://orcid.org/0000-0003-1490-4521>

Nathan Briggs

National Oceanography Centre

Peter Strutton

Institute for Marine and Antarctic Studies

Philip Boyd

University of Tasmania <https://orcid.org/0000-0001-7850-1911>

---

## Article

**Keywords:** particulate organic carbon, particle injection pumps, biological gravitational pump

**Posted Date:** November 17th, 2021

**DOI:** <https://doi.org/10.21203/rs.3.rs-1006941/v1>

**License:**  This work is licensed under a Creative Commons Attribution 4.0 International License.

[Read Full License](#)

---

1 **Multi-year robotic observations reveal the seasonality of downward carbon**  
2 **export pathways in the Southern Ocean**

3 **Authors:** Léo Lacour<sup>1,2\*</sup>, Joan Lloret<sup>3</sup>, Nathan Briggs<sup>4</sup>, Peter G. Strutton<sup>1,5</sup>, Philip W. Boyd<sup>1</sup>

4 **Affiliations:**

5 <sup>1</sup> Institute for Marine and Antarctic Studies, University of Tasmania, Hobart, Australia

6 <sup>2</sup> Sorbonne Université, CNRS, Laboratoire d'Océanographie de Villefranche, LOV,  
7 Villefranche-sur-Mer, France

8 <sup>3</sup> Barcelona Supercomputing Center, Earth Sciences Dept., Barcelona, Spain

9 <sup>4</sup> National Oceanography Centre, Southampton, UK.

10 <sup>5</sup> Australian Research Council Centre of Excellence for Climate Extremes, University of  
11 Tasmania, Hobart, Australia

12 \*Correspondence to: [leo.lacour@utas.edu.au](mailto:leo.lacour@utas.edu.au)

13

14 **Introductory paragraph**

15 At high latitudes, the export of organic matter from the surface to the ocean interior, the  
16 biological carbon pump, has conventionally been attributed to the gravitational sinking of  
17 particulate organic carbon (POC). Conspicuous deficits in ocean carbon budgets have recently  
18 challenged this long-lived paradigm of a sole pathway. Multiple strands of evidence have  
19 demonstrated the importance of additional export pathways, including the particle injection  
20 pumps (PIPs). Recent model estimates revealed that PIPs have a comparable downward POC  
21 flux to the biological gravitational pump (BGP), but with potentially different seasonal  
22 signatures. To date, logistical constraints have prevented concomitant and extensive  
23 observations of these pumps, and little is known about the seasonality of their fluxes. Here,  
24 using year-round robotic observations and recent advances in optical signal analysis, we  
25 concurrently investigated the functioning of two PIPs - the mixed layer and eddy subduction  
26 pumps - and the BGP in Southern Ocean waters. By comparing three phytoplankton bloom  
27 cycles in contrasting environments, we show how physical forcing and phytoplankton

28 phenology influence the magnitude and seasonality of these pumps, with implications for  
29 carbon sequestration efficiency.

30

31

32 The biological carbon pump (BCP) is considered a major contributor to the Southern Ocean  
33 (SO) carbon sink. It removes 3 PgC from the euphotic zone (Ez, upper ~100 m) annually,  
34 representing 33% of the global BCP<sup>1</sup>. Since the concept of the BCP was originally proposed<sup>2</sup>,  
35 it has been widely assumed that it was mediated primarily by the sinking of POC, now called  
36 the Biological Gravitational Pump (BGP)<sup>3</sup>. However, current estimates of biological carbon  
37 demand in the mesopelagic (~100-1000 m depth) exceed carbon inputs attributed to sinking  
38 material from the euphotic zone by two- to three- fold<sup>4</sup>. Such discrepancies highlight the need  
39 to reassess the pathways that contribute to downward carbon export.

40 Recently, other particle injection processes have been invoked as additional pathways that help  
41 to balance the carbon budget in the mesopelagic<sup>3</sup>. Studies<sup>5-7</sup> have provided evidence that  
42 downward export of organic matter also occurs through localized (1-10 km) eddy-driven  
43 subduction of POC. This process, known as the Eddy Subduction Pump (ESP), leads to episodic  
44 injection of POC-rich waters below the mixed layer. Similarly, the cycle of deep vertical mixing  
45 and re-stratification events during the winter to spring transition acts as a physical pump that  
46 injects fresh organic matter into the mesopelagic, the so-called mixed layer pump (MLP)<sup>8,9</sup>. At  
47 basin scale, the ESP and MLP are equivalent to about one quarter of the BGP export<sup>3</sup>. However,  
48 at the (sub)mesoscale (<100 km) these processes can be equal to, or even greater than the  
49 BGP<sup>10,11</sup>. This spatial mismatch illustrates the difficulty of carrying out comprehensive  
50 intercomparison of these pumps in the field. The mesopelagic migrant pump<sup>12</sup>, seasonal lipid  
51 pump<sup>13</sup> and large-scale subduction<sup>14</sup> pump are also important contributors to the BCP, although  
52 assessing their relative contribution is even more challenging<sup>3</sup> and beyond this study.

53 Boyd et al. (2019)<sup>3</sup> suggested that the relative importance of both the PIPs and BGP varies  
54 seasonally, resulting in substantially different fates for exported carbon with respect to depth of  
55 remineralisation, sequestration time scale, and consumption by midwater biota<sup>10</sup>. However,  
56 concomitant and extensive observations of these pumps are extremely rare, and little is known  
57 about the seasonality of their fluxes. Better characterisation of these pumps and their seasonality

58 will fundamentally push forward our understanding of ocean biological carbon export and  
59 sequestration, and help to close regional ocean carbon budgets.

60 Biogeochemical-Argo (BGC-Argo) floats with multi-year missions and high frequency  
61 sampling offer a promising way to jointly investigate the PIPs and the BGP over a broad range  
62 of time and space scales. Such platforms have already been successfully used to characterise  
63 the MLP at sub-seasonal to seasonal scales<sup>8,9</sup>, the ESP at pan-Antarctic scale<sup>6</sup>, and the  
64 seasonality of the BGP<sup>15,16</sup>. In this work we refine and bring together a range of previously  
65 developed techniques. Concurrent measurements of chlorophyll *a* fluorescence and particulate  
66 backscattering (proxies of phytoplankton biomass and POC, respectively), oxygen, temperature  
67 and salinity have been used to identify subsurface anomalous features related to the MLP and  
68 ESP<sup>5,17</sup>. Spikes in particulate backscattering and chlorophyll *a* fluorescence have provided  
69 insights into the sinking of aggregates through the mesopelagic<sup>18</sup> while short term (order of  
70 days) particle accumulation on transmissometer sensors, working as optical sediment traps  
71 (OST)<sup>19</sup>, allowed characterising the BGP. This novel combination of approaches links a  
72 bespoke sensor constellation with recent advances in optical signal analysis to compare the  
73 BGP with two PIPs - the MLP and the ESP - through three annual cycles. We focus on a single  
74 float, which sampled contrasting biogeochemical provinces across the Pacific sector of the SO,  
75 to infer the causal mechanisms that set the magnitude and seasonality of each of these pumps.  
76 These mechanisms include bloom timing or seasonality, hereafter called phenology, which  
77 influences the concentration, size and composition of the particle assemblage in the upper  
78 ocean.

79

## 80 **Characteristics of the particle assemblage in contrasting environments**

81 We present here *in situ* observations collected by a BGC-Argo float (WMO 7900791) that  
82 travelled >6000 km across the Pacific sector of the SO (Fig. 1a). This float was deployed in  
83 May 2016 in sub-polar waters and sampled the water column from 500 m to the surface every  
84 1 to 5 days during three annual cycles. It crossed the Polar Front in September 2016 as  
85 evidenced by the abrupt decrease in surface temperature (from 6°C to 3°C, Fig. 1c). The float  
86 remained in the vicinity of the Polar Front for almost an entire year, until July 2017, and then  
87 entered polar waters where near-zero surface temperatures were observed. It was in the vicinity  
88 of the sea-ice edge from June to August 2018 (Fig. 1b) in an area characterized by very low  
89 salinity surface waters (Fig. 1d) which prevented any deep mixing events during winter. Indeed,

90 the mixing layer depth ( $MLD_{bio}$ , see Methods) remained shallow ( $<100$  m) as opposed to the  
91 two previous winters where mixing reached 250-350 m (the black thick line in Fig 1c,d). The  
92 float ended its mission due to battery failure in Drake Passage in May 2019. This long trajectory  
93 across different oceanic provinces enabled us to characterize the pumps over a broad range of  
94 time and space scales in contrasting environments. The downside is the difficulty to study the  
95 seasonality of these pumps when the float moves across different water masses. We therefore  
96 segmented the trajectory into three bloom cycles during which the contiguous nature of water  
97 masses was verified (Fig. S2 and Methods).

98 These contrasting environments corresponded to clear contrasts in bio-optical proxies for  
99 concentration, size and composition of phytoplankton community and associated particles  
100 between the three bloom cycles recorded (Fig. 2). The 2016-17 bloom, near the Polar Front,  
101 was the most intense as reflected in POC (up to  $175 \text{ mg C m}^{-3}$ , Fig. 2a) and chlorophyll *a*  
102 fluorescence ( $F_s$  around  $1 \text{ mg m}^{-3}$  chlorophyll, Fig. S7). This bloom was characterised by a very  
103 low fluorescence to backscattering ratio,  $F_s / b_{bs}$  (where *s* denotes the small fraction of particles,  
104 see Methods), a ratio which varies according to changes in phytoplankton community structure,  
105 photoacclimation and nutrient status<sup>20-22</sup>. Here, we attribute low  $F_s / b_{bs}$  values to the growth of  
106 coccolithophores, calcifying phytoplankton which form liths – bio-mineral shells – with high  
107 refractive index and thus high backscattering signal<sup>23</sup>. Coccolithophore blooms are recurrent  
108 features in the SO, readily detectable from space<sup>24,25</sup>. Indeed, satellite records confirmed the  
109 presence of an intense coccolithophore bloom during this summer in the area where the float  
110 was profiling (Fig. S4). Bio-minerals act as ballast by increasing particle specific gravity and  
111 sinking speeds, and provide protection from remineralisation<sup>26</sup>, potentially explaining the  
112 massive invasion of POC to 450 m following the coccolithophore bloom (Fig. 2a).

113 The 2017-18 bloom was less intense with lower phytoplankton biomass. It was characterised  
114 by a high  $F_s / b_{bs}$  at its peak (apex), when the mixing layer abruptly shoaled from 300 to  $<100$   
115 m (Fig. 2a, b). Such high  $F_s / b_{bs}$  ratios associated with high-latitude spring blooms, when light  
116 is not limiting (Fig. S5), have been attributed to diatom-dominated events<sup>20,21</sup>, which in this  
117 case would have benefited from iron inputs by winter deep mixing and melt waters (Fig. 1c, d).  
118 However, the float-derived iron limitation index<sup>27</sup> (Fig. S5 and Methods) indicates that in late  
119 December 2017 iron was rapidly depleted by biological consumption, resulting in low  
120 phytoplankton biomass relative to the 2016-17 and 2018-19 blooms. Accordingly, the size of  
121 particles/aggregates was two-fold lower than for the 2016-17 bloom (Fig. 2c and Methods), but  
122 still two-fold higher than the 2018-19 bloom where higher biomass levels were observed.

123 Diatoms dominating the 2017-18 bloom may explain the relatively high mean particle size. The  
124 transition of the bloom to a subsurface chlorophyll maximum (SCM) feature was another  
125 indication of nutrient limitation. High  $F_s / b_{bs}$  at the SCM (around ~125 m depth, Fig. 2b) was  
126 due to photoacclimation as light became limiting in the subsurface. In April 2018, the  
127 photoacclimation signal propagated in the entire mixing layer as light levels continued  
128 decreasing (Fig. S5) and convective mixing commenced again (Fig. S1b, c).

129 The 2018-19 bloom was partially sampled as data were missing for nearly two months early in  
130 the productive season. The SCM observed from December to February 2018 (Fig. 2b),  
131 relatively small particles in the surface layer (Fig. 2c), and a high iron limitation index (Fig. S5)  
132 suggest that the bloom was at a late stage when sampled, characteristic of open-water conditions  
133 in the seasonal sea-ice zone<sup>28</sup>. The second intense peak of biomass recorded in April 2019  
134 developed in the Drake Passage, near the Antarctic Peninsula, a region known to be influenced  
135 by iron-enriched shelf waters<sup>29</sup>. Accordingly, the iron limitation index dropped to low values  
136 similar to those observed during the first 2016-17 bloom (Fig. S5).

137

### 138 **Seasonality of multiple carbon export pathways**

139 The sensor constellation on the BGC-Argo float was used to independently assess the  
140 seasonality of the BGP and to concurrently explore the timing of MLP and ESP events. The  
141 BGP was characterised by two independent methods, namely the spike index and the OST (see  
142 Methods). The spike index quantifies the abundance of large particles in the water column, from  
143 both fluorescence and backscattering ( $F_l$  and  $b_{bl}$  respectively, where  $l$  denotes large fraction of  
144 particles, Fig. 3b, S10 and Methods).  $F_l$  was attributed to live phytoplankton aggregates sinking  
145 through the water column and represents a subset of  $b_{bl}$  which also includes fecal and detrital  
146 matter<sup>18</sup>. These two components were decoupled in time during the 2016-17 bloom. Prior to the  
147 maximum in POC (early January, Fig 3a), the dominance of the  $F_l$  spike index was attributed  
148 to a diatom bloom that generally precede coccolithophore blooms<sup>30</sup>. Indeed, diatom export  
149 events have often been described as an initial pulse of fresh aggregates<sup>18</sup> followed by a second  
150 pulse of resting spores, empty frustules and fecal pellets<sup>31</sup>, the latter explaining the significant  
151 peak in the  $b_{bl}$  spike index observed in mid-December, before the maximum in POC attributed  
152 to the coccolithophore bloom. Low  $F_l$  and maximum  $b_{bl}$  spike indices in mid-January 2017  
153 following the coccolithophore bloom resulted from sinking aggregates partly made of detached  
154 coccoliths<sup>32</sup>. A decoupling in  $F_l$  and  $b_{bl}$  spike indices was also evident during the 2017-18

155 diatom bloom. However, the spike index was low relative to the 2016-17 bloom. It is likely that  
156 lower surface biomass during the 2017-18 bloom (Fig. 2a) led to lower levels of aggregation<sup>33</sup>,  
157 as evidenced by the lower peak mean particle size (Fig. 2c). Conversely,  $F_1$  and  $b_{bl}$  spike indices  
158 were coupled during the 2018-19 bloom (second peak of biomass in April 2019) with the  $b_{bl}$   
159 spike index as the main contributor (Fig. 3b). In all three blooms,  $F_1$  was rapidly attenuated with  
160 depth while  $b_{bl}$  remained high as deep as 450 m (Fig. S6) as a result of higher fragmentation  
161 and/or consumption rates of fresh and fragile phytoplankton aggregates than of other large  
162 sinking particles<sup>18</sup>.

163 The OST method provides the opportunity of measuring an *in situ* BGP flux from autonomous  
164 floats (see Methods). These measurements are however limited to a single depth, the float  
165 ‘parking’ depth, here ~300 m, and are not calibrated in terms of carbon biomass, so they are  
166 expressed in  $d^{-1}$  <sup>19,34</sup>. This flux was divided into two components, a continuous flux of small  
167 slow-sinking particles (slowly accumulating on the transmissometer window) and a pulsed flux  
168 of large fast-sinking particles (creating discontinuities in transmissometer records)<sup>19</sup>. The 2016-  
169 17 bloom illustrates well the decoupling between the continuous and pulsed fluxes (Fig. 3c).  
170 The latter peaked in mid-January when we observed maximum  $b_{bl}$ , while the continuous flux  
171 peaked ~20 days later in early February 2017. Assuming both fluxes followed the early January  
172 peak in mixing layer POC, the estimated sinking speeds of large (pulsed flux) and small  
173 (continuous flux) particles were ~30  $m d^{-1}$  and ~10  $m d^{-1}$  respectively. These values are in  
174 agreement with measured sinking speeds of coccolithophore blooms<sup>32</sup>. The delay between the  
175 continuous and pulsed flux may also reflect disaggregation processes in the mesopelagic which  
176 have been reported to account for half of the flux attenuation at high latitudes<sup>18</sup>. Following the  
177 2017-18 diatom bloom, the low pulsed flux at 300 m was consistent with a high contribution of  
178 fresh aggregates ( $F_1$  spike index >80% of the total  $F_1 + b_{bl}$  spike index until early December)  
179 which were rapidly consumed in the upper mesopelagic, fragmented into smaller particles, and  
180 later detected in the continuous flux record (Fig. S12). Note the relatively high continuous flux  
181 in late summer and fall when mixing layer POC (Fig. 3a) and particle size (Fig. 2b) were close  
182 to the annual minimum. This finding suggests that small low-light low-nutrient adapted  
183 phytoplankton contributed ~50% of the annual continuous flux through slow-sinking of small  
184 particles<sup>35</sup> (Fig. S12).

185 The ESP contribution to the BCP was quantified as the inventory of POC measured in  
186 subsurface anomalous features attributed to localized subduction events<sup>6</sup> (Fig. S9 and  
187 Methods). Such features were detected only during 2016-17 in the vicinity of the Polar Front

188 (Fig. 3d), a highly energetic region prone to (sub)mesoscale circulation and ESP events<sup>6</sup>. We  
189 indeed observed strong spice anomalies (density-compensated changes in temperature and  
190 salinity; Fig. S1d, S2 and Methods) over the entire water column revealing different water  
191 masses interleaving. The most intense ESP events occurred early in the productive season  
192 (September-October 2016), prior to the bloom climax (Fig. S12). Thus, these ESP events  
193 actively transported small and freshly-produced organic material as deep as ~400 m (Fig. 2c,  
194 3d and S13). Such labile particles would likely not have reached these depths via the BGP,  
195 which illustrates the biogeochemical significance of the ESP. A second peak in ESP events  
196 occurred concurrently with the main peak in the  $F_i$  spike index (early December 2016)  
197 suggesting that the ESP also transports large fresh aggregates produced in the Ez, in addition to  
198 small suspended particles and dissolved compounds<sup>9</sup>.

199 As for the ESP, the MLP was quantified as the inventory of POC measured in MLP remnant  
200 layers, delimited by  $MLD_{bio}$  at the top and  $MLD_{dens}$  at the bottom (Fig. S11 and Methods).  
201  $MLD_{dens}$  was defined as the maximum vertical density gradient, and refers to the depth of the  
202 seasonal pycnocline<sup>8</sup>. All MLP events occurred prior to the bloom apex, each year (Fig. 3d and  
203 S12), during the transition between winter deep mixing and spring stratification (~3 months).  
204 The strong sub-seasonal variability of the mixing layer depth in 2017 (from 50 to 300 m, Fig.  
205 S11), with intermittent stratification and deep mixing events, efficiently transferred organic  
206 material out of the mixing layer to depth. Relatively high  $F_s$  content in the remnant layer, as  
207 deep as 350 m (Fig. S11), demonstrates the freshness of the exported material, of which a  
208 fraction was potentially permanently isolated from the mixing layer<sup>8</sup>. The timing of MLP events  
209 with respect to bloom timing suggests that large particles produced in the Ez (e.g. in November  
210 2017, Fig. 2c) can also be actively transferred to depth, similar to that observed for the ESP.  
211 These results illustrate the possible interplay between a PIP and the BGP, where gravitational  
212 sinking could take over downward export following a physical injection event.

213

## 214 **Implications for oceanic carbon storage**

215 Multi-year and high-resolution float observations provide a new and more comprehensive view  
216 of the various pumps that contribute to the BCP over the annual cycle. The main insight from  
217 our study is the seasonal succession of processes contributing to the export of organic carbon  
218 to the deep ocean. Export due to the ESP was observed early in the bloom, before the bloom  
219 climax, and again at the bloom apex. The MLP was most active during the seasonal transition

220 from deep mixing to stratification, and again during sub-seasonal stratification events. Finally,  
221 the gravitational pulsed flux was most intense at the bloom apex, while the continuous flux  
222 persisted throughout the year, with maximum values delayed in time with respect to the bloom  
223 apex – in fall in the case of the 2017-18 bloom. The contribution of all these processes over a  
224 complete annual cycle should definitely be accounted for when computing regional  
225 mesopelagic carbon budgets.

226 Another important insight is the identification of the depth strata for the potential interplay  
227 between the PIPs and BGP<sup>3</sup>. Float-derived optical proxies revealed that PIPs inject large fresh  
228 aggregates as deep as 400 m, which then can sink further through gravitational sinking<sup>36</sup>. The  
229 MLP and ESP have the capacity to transport organic matter at vertical velocities of order of  
230 100-1000 m d<sup>-1</sup> <sup>37,38</sup>, while sinking speeds are order of 10-100 m d<sup>-1</sup> for large aggregates<sup>18,39</sup>.  
231 Thus, physically-mediated processes accelerate the transit through the main remineralisation  
232 horizon. The interplay between the PIPs and BGP makes it challenging to assess their relative  
233 contribution to carbon sequestration, but the overlap that we find in their timing clearly suggest  
234 that their joint contributions can boost the overall efficiency of the BCP.

235 Large-scale estimates of the PIP contribution to carbon storage require regional high-resolution  
236 models able to simulate some of the complex BCP mechanisms we observed<sup>11,36</sup>. However, to  
237 provide reliable results these models need a larger number of high-resolution, multi-year  
238 observations. Process-focused biogeochemical floats with high-frequency sampling are the  
239 most cost-effective solution for providing these observations. By combining widespread high-  
240 resolution observations with fit-for-purpose models of the full suite of export processes, it  
241 should be possible to develop advanced parameterizations that incorporate contemporaneous  
242 knowledge of the BCP into Earth System Models with minimal computational cost.

243

## 244 **Methods**

### 245 **Float data processing**

246 The BGC-Argo float used is a Teledyne Webb Research APEX float, equipped with a Sea-Bird  
247 SBE41 CTD sensor, WET Labs ECO fluorometer and scattering sensors measuring chlorophyll  
248 *a* fluorescence and the volume scattering function (at ~124°, 470 and 700 nm wavelengths), a  
249 Satlantic OC4 radiometer measuring downwelling irradiance at 412, 443, 490 and 550 nm, an  
250 Aanderaa Oxygen Optode, and a WET Labs C-Rover transmissometer (660 nm).

251 The CTD and trajectory data were quality-controlled using the standard Argo protocol<sup>40</sup>. ECO  
252 raw signals were converted to chlorophyll *a* fluorescence (F, in mg Chl m<sup>-3</sup>) and particulate  
253 backscattering coefficient ( $b_{bp}$  in m<sup>-1</sup>) following the BGC-Argo procedures<sup>41,42</sup>. Bio-optical data  
254 were quality-controlled following the BGC-Argo quality control manual<sup>43</sup>. In addition, F was  
255 corrected from the non-photochemical quenching (NPQ) following Xing et al. (2018)<sup>44</sup>. Briefly,  
256 for each profile where the sun elevation angle was  $> 5^\circ$ , the maximum F value above the mixed  
257 layer depth, defined here as a density difference of 0.01 kg m<sup>-3</sup> with a reference value at 5 m,  
258 was extrapolated toward the surface. As an additional condition, the depth of the extrapolated  
259 F value had to be shallower than the 15  $\mu\text{mol photons m}^{-2} \text{s}^{-1}$  isolume<sup>44</sup>. As the instantaneous  
260 Photosynthetically Available Radiation (iPAR) was not directly measured, we estimated iPAR  
261 profiles from the measured downwelling irradiance at 4 wavelengths. At each depth, a spline  
262 interpolation was used to compute the irradiance spectra from 400 to 1000 nm (with irradiance  
263 value set to zero at 1000 nm). iPAR was then calculated by integrating the interpolated  
264 irradiance spectra from 400 to 700 nm. Oxygen data were calibrated using air measurements  
265 following Johnson et al. (2015)<sup>45</sup>, with a mean gain factor of 1.0557. The  $b_{bp}$  at 700 nm was  
266 converted into particulate organic carbon (POC) following the relationship in Johnson et al.  
267 (2017)<sup>46</sup>. Similarly, the  $b_{bp}$  at 470 nm was converted into phytoplankton carbon biomass ( $C_{\text{phyto}}$ )  
268 following the relationship in Graff et al. (2015)<sup>47</sup>. Note that the presence of coccolithophores  
269 during the 2016-17 bloom elevates  $b_{bp}$  without necessarily elevating POC or  $C_{\text{phyto}}$ , potentially  
270 leading to overestimation of these carbon estimates.

271 The float mission included CTD and bio-optical profiles every 1.5 to 6 days, from 500 m to the  
272 surface, with a parking depth of 300 m. The vertical sampling resolution ranged from 3 to 10  
273 m depending on the float ascent speed. All profile data were interpolated at 1 m resolution.

#### 274 **Quasi-Lagrangian framework**

275 During its 36-month mission, the float visited different oceanic provinces and crossed strong  
276 water mass boundaries, such as in September 2016 when the float crossed the Polar Front. Thus,  
277 observed changes in biogeochemical properties are not solely due to temporal changes, making  
278 the study of the seasonality of these properties hazardous. We therefore divided the timeseries  
279 into three periods in which the contiguous nature of the water masses was verified based on  
280 temperature and salinity properties (24-Sep-2016 to 22-May-2017; 10-Oct-2017 to 7-Jun-2018;  
281 5-Nov-2018 to 1-May-2019; Fig. S3). The absence of strong water mass contrasts allows us to  
282 assume a quasi-Lagrangian framework, where changes in biogeochemical properties can be

283 interpreted as temporal changes. This approach is commonly used in float studies<sup>48–50</sup>. For  
 284 completeness, the figures show the full float timeseries, but only the three quasi-Lagrangian  
 285 periods are discussed in the text. When calculating rate of change with respect to time (see  
 286 Methods’ section “Phenology metrics”), the timeseries of the biogeochemical properties of  
 287 interest were first linearly interpolated on equally spaced 5-day timeseries, and then  
 288 smoothed with a 30-day (7 points) running average to filter out short-term fluctuations and  
 289 focus on seasonality.

## 290 Mean particle size

291 Mean particle diameter in the upper 50 m, weighted by particle cross-sectional area, was  
 292 estimated from high-frequency variations in  $b_{bp}$  and  $c_p$  using the variance-to-mean ratio  
 293 method<sup>51</sup>, adapted for use on profiling floats following Rembauville et al. (2017)<sup>21</sup>. This method  
 294 extracts particle size information from the “spikiness” of optical profiles where particle  
 295 concentrations are too high to separate individual spikes from a small-particle baseline. Briefly,  
 296 mean diameter was estimated from  $c_p$  via Eq. (1):

$$297 \quad \bar{A}_{cp} = \frac{\text{var}(c_p \text{ detrended})}{\text{mean}(c_p)} \frac{V}{Q_c} \frac{1}{\alpha(\tau)} \quad (1)$$

$$298 \quad \alpha(\tau) = \begin{cases} 1 - (3\tau)^{-1}, & \text{if } \tau \geq 1 \\ \tau - \tau^2/3, & \text{if } \tau \leq 1 \end{cases}$$

$$299 \quad \tau = \left( \frac{t_{res}}{t_{samp}} \right)$$

$$300 \quad \bar{D}_{cp} = 2 \sqrt{\bar{A} \pi^{-1}}$$

301 where  $t_{res}$  is the residence time of a particle in the sample volume (0.1 s),  $t_{samp}$  is the duration of  
 302 a single measurement (1 s),  $V$  is the transmissometer sample volume (12.5 ml),  $Q_c$  is the optical  
 303 attenuation efficiency of the particles (assumed to be 2 following Bohren and Huffman, 1983<sup>52</sup>),  
 304  $\text{var}(c_p \text{ detrended})$  is the variance of  $c_p$  after detrending using an 5-point running median, and  $D_{cp}$  is  
 305 the area-weighted mean particle diameter. The calculation was then repeated for  $b_{bp}$  at both 470  
 306 and 700 nm, by replacing  $c_p$  with  $b_{bp}$  in Eq. 1, and using  $V = 0.62$  ml (Briggs et al., 2013),  $t_{samp}$   
 307 = 1 s,  $t_{res} = 0.06$  s, and  $Q_{bb} = 0.02$ <sup>51</sup>. In order to reduce “noise” in the individual size estimates,  
 308 the three estimates were then combined together into 10 d bins, whose medians and 25<sup>th</sup> and  
 309 75<sup>th</sup> percentiles are reported here.

## 310 Spike index

311 F and  $b_{bp}$  were partitioned into 3 components as in Briggs et al. (2020)<sup>53</sup>: deep sensor blanks,  
312 including a background of small refractory particles ( $b_{br}$  and  $F_r$ ); small, labile backscattering  
313 ( $b_{bs}$ ) and fluorescing ( $F_s$ ) particles; and large, fast-sinking backscattering ( $b_{bl}$ ) and fluorescing  
314 ( $F_l$ ) particles (see supplementary materials in Briggs et al. (2020)<sup>53</sup> for details on this  
315 partitioning). Temporal sections of  $F_l$  and  $b_{bl}$  at 470 and 700 nm are shown in supplementary  
316 figure S10. The spike index was computed by depth-integrating  $F_l$  and  $b_{bl}$  from the mixing layer  
317 depth to 500 m, and then normalising by their minimum and maximum values. This index  
318 makes it possible to quantify the amount of large, fast-sinking particles present in the water  
319 column. For the sake of simplicity, only the  $b_{bl\ 470}$  spike index is shown in figure 3. The  $b_{bl\ 700}$   
320 spike index shows similar results.

### 321 **Optical sediment trap**

322 The Optical Sediment Trap (OST) method uses the rate of change of particle attenuation ( $-\ln(\text{transmittance})$ , unitless) during the float drifting period at the parking depth of 300 m<sup>16,19,34</sup>.  
323 The accumulation of small slow-sinking particles onto the upward-facing window of the  
324 transmissometer drives a smoothly increasing attenuation while the accumulation of large fast-  
325 sinking particles produces discontinuities in transmissometer records. Both signals were  
326 converted into a continuous flux and a pulsed flux (in units of  $d^{-1}$ ), respectively, following  
327 procedures described in Estapa et al. (2013, 2017)<sup>19,34</sup> with few modifications to take into  
328 account the use of a different platform with different parking behaviour and sampling frequency  
329 (every 1h in this study). First, parking phases of duration  $< 24h$  were not considered to ensure  
330 a sufficient number of data points. The first 3 data points (3h) were removed from the analysis  
331 as the float takes time to stabilize at the target depth. Optical spikes, defined as an increase in  
332 beam attenuation of  $0.002\ h^{-1}$  followed by a decrease within 3h, were also removed and a 5-  
333 point median filter was applied. Then, the remaining data points were divided into linear  
334 segments interspersed with discontinuities, or ‘jumps’, following the procedure in Estapa et al  
335 (2013)<sup>34</sup>, except that discontinuities were not identified a priori with a threshold criteria but  
336 resulted from the subdivision of segments not meeting the fitting criteria. For each parking  
337 phase, the continuous flux of slow-sinking particles was computed as the mean slope of all  
338 linear segments weighted by their length. The pulsed flux was computed as the sum of all  
339 positive discontinuities normalized by the duration of the parking phase.  
340

### 341 **Mixed layer pump**

342 The detection of episodic Mixed Layer Pump (MLP) events follows the methodology described  
343 in Lacour et al. (2019)<sup>17</sup>. The basis of this method is to distinguish between the mixed layer,  
344 the zone of relatively homogeneous water formed by the history of mixing, and the mixing  
345 layer, the zone in which mixing is currently active. The mixed and mixing layer depths were  
346 computed as the maximum vertical gradient of density ( $MLD_{dens}$ ) and chlorophyll *a*  
347 fluorescence ( $MLD_{bio}$ ), respectively. The underlying concept is that chlorophyll *a* fluorescence,  
348 as a proxy of phytoplankton biomass, is homogeneous over the whole mixing layer if turbulent  
349 mixing overcomes vertical variations in phytoplankton net growth rate<sup>54</sup>. During the winter to  
350 spring transition,  $MLD_{bio}$  is generally shallower than  $MLD_{dens}$  and varies at higher frequency  
351 ( $\sim 1$ -2 days for  $MLD_{bio}$  and  $\sim 10$  days or more for  $MLD_{dens}$ ) in response to changes in  
352 atmospheric forcing (Fig. S11). On a single float profile, the formation of a remnant layer,  
353 delimited by  $MLD_{bio}$  at the top and  $MLD_{dens}$  at the bottom, can be easily identified and used as  
354 a signature of a recent MLP event. To quantify the amount of carbon exported to the  
355 mesopelagic by MLP events, each POC profile was depth-integrated over the remnant layer,  
356 where organic matter was potentially trapped. To avoid accounting for POC initially present in  
357 the mesopelagic, the mean POC value from  $MLD_{dens}$  to 500 m was subtracted from the POC  
358 profile before the depth integration. Note that in the presence of SCM, typically in summer,  
359  $MLD_{bio}$  can be deeper than the mixing layer depth and corresponds more likely to the base of  
360 the euphotic zone.

### 361 **Eddy subduction pump**

362 To detect the subduction events contributing to the ESP, we used an updated version of the  
363 detection method described in Llorc et al. (2018)<sup>6</sup>. This method relies on the fact that vertical  
364 extent of submesoscale features that drive ESP is of the order of  $\sim 10$  m and can be smoothed  
365 out by averaging float's vertical variability over larger vertical scales. We applied a 20-bin  
366 running average over profiles at 5 m vertical resolution. As a result, we obtained submesoscale-  
367 free vertical variability that can be compared to the original profiles to identify anomalous  
368 features. We focused only on anomalies found between the bottom of the mixing layer depth  
369 and 500 m. As anomalies can be related to other mechanisms than submesoscale vertical  
370 circulation, individual profiles were classified as an ESP event if negative anomalies of  
371 Apparent Oxygen Utilisation (AOU') and spice ( $\pi'$ ) coincided in depth. To define the relevant  
372 anomalies, we applied detection thresholds to only consider anomalies with  $AOU' < -8 \mu\text{mol}$   
373  $\text{kg}^{-1}$  and  $\pi' < -0.1$ . We have also modified the method to better constrain the thickness of the  
374 anomalous features, an important metric to estimate the amount of POC exported. In the current

375 version, we detected the top and bottom depths of both AOU' and  $\pi'$  as the first and last bin  
376 depths where the anomalies were still negative. We then compared the detected depths on AOU  
377 and  $\pi'$  to define the deepest (shallowest) of the two as the anomaly bottom (top) depth.

### 378 **Iron stress index**

379 The iron stress index was computed following the method in Ryan-Keogh & Thomalla (2020)<sup>55</sup>.  
380 The concept of this method is that NPQ variability is linked to iron and light availability and  
381 has the potential to provide important diagnostic information on phytoplankton physiology<sup>56</sup>.  
382 To remove the effect of in situ light availability on NPQ variability, Ryan-Keogh & Thomalla  
383 (2020)<sup>55</sup> proposed to compute  $\alpha_{NPQ}$  the initial slope of the NPQ-PAR curve. Thereby,  $\alpha_{NPQ}$   
384 could be used as a proxy for iron limitation, with higher values being associated with greater  
385 iron stress. In our study, NPQ as a function of depth was quantified as the difference between  
386 the quenching corrected fluorescence profile and the quenched one, normalized by the latter.  
387 For each profile, we plotted our iPAR estimates against NPQ values. We then applied a linear  
388 fit to the NPQ-iPAR curve in the region of low iPAR values (between 15 and 75  $\mu\text{mol photons}$   
389  $\text{m}^{-2} \text{s}^{-1}$ ), where the slope of the linear fit gives  $\alpha_{NPQ}$ . Linear fits with  $R^2 < 0.8$  were rejected (1%  
390 of the profiles). We did not fit a Platt-like model as in Ryan-Keogh & Thomalla (2020)<sup>55</sup>  
391 because our iPAR values were too low to induce a saturation plateau and because we were  
392 interested only in the initial slope of the NPQ-iPAR curve. Note that  $\alpha_{NPQ}$ , as a proxy for iron  
393 limitation, has to be interpreted with caution as shifts in phytoplankton community composition  
394 and changes in the light regime and thus phytoplankton photoacclimation status impact the  
395 variability of  $\alpha_{NPQ}$ <sup>57,58</sup>. For that reason, we also computed the median light level within the  
396 mixing layer ( $I_{ML} = PAR_{SAT} e^{-0.5 K_d(PAR) MLD_{bio}}$ ) which is often used in photoacclimation  
397 models<sup>59</sup>. Here,  $PAR_{SAT}$  is the daily mean PAR from MODIS Aqua (4 km) and  $K_d(PAR)$  is the  
398 diffuse attenuation coefficient of PAR (in units of  $\text{m}^{-1}$ ).  $K_d$  was first computed at 490 nm by  
399 fitting a fourth-degree polynomial function to the logarithm of the downwelling irradiance  
400  $E_{d(490)}$  as a function of depth, measured by the float, and then calculating the mean slope over  
401 the first 50 m<sup>60,61</sup>.  $K_{d(490)}$  was then converted to  $K_d(PAR)$  following equation 9 in Morel et al.  
402 (2007)<sup>62</sup>. We did not find a clear relationship between  $I_{ML}$  and  $\alpha_{NPQ}$  (Fig. S5). The influence of  
403 shifts in phytoplankton community composition on  $\alpha_{NPQ}$  variability cannot be ruled out, but it  
404 is worth noting that phytoplankton community also shifts in response to iron availability<sup>63</sup>.

### 405 **Phenology metrics**

406 Phytoplankton phenology can be characterised by three metrics<sup>64</sup>: (i) the bloom onset when  
407 bulk phytoplankton biomass starts accumulating (i.e. when the accumulation rate  $r$  changes  
408 from negative to positive value), (ii) the bloom climax when  $r$  reaches its annual maximum  
409 value, (iii) the bloom apex when bulk phytoplankton biomass  $P$  reaches its annual maximum  
410 value. Following Uchida et al. (2019)<sup>65</sup>,  $P$  was estimated by vertically integrating  $C_{\text{phyto}}$ , derived  
411 from the backscattering, over the whole water column. To avoid including non-phytoplankton  
412 particulate matter (e.g. refractory material) in the calculation,  $C_{\text{phyto}}$  was masked out at depths  
413 where  $F_s = F - F_l - F_r \leq 0$ , where  $F_r = 0.03 \text{ mg m}^{-3}$  (Fig. S7). The accumulation rate was then  
414 calculated as  $r = \frac{1}{P} \frac{\delta P}{\delta t}$ . The bloom onset and apex were used as milestones to compare the  
415 timing of the 2016-17 and 2017-18 blooms with the seasonality of the carbon export pathways  
416 (Fig. S12). The time axis in Figure S12 was rescaled by the onset and the apex of the bloom, so  
417 that 0 corresponds to the onset and 1 to the apex.

418

## 419 **Acknowledgements and data availability statement**

420 LL was supported by a European Union's Horizon 2020 Marie Skłodowska-Curie grant (no.  
421 892653). Visits by LL to IMAS/UTas were supported by the Australian Research Council  
422 Special Research Initiative for Antarctic Gateway Partnership (Project ID SR140300001), the  
423 Australian Research Council Centre of Excellence for Climate System Science (Project ID  
424 B0018492), and the UTas visiting scholar program. JL was supported by the European Union's  
425 Horizon 2020 research and innovation programme under the Marie Skłodowska-Curie grant  
426 agreement No. 754433. PS was supported by the Australian Research Council Centre of  
427 Excellence for Climate Extremes (Project ID P0023578). PWB was funded by the Australian  
428 Research Council by Laureate Fellowship FL160100131. BGC-Argo data used in this study  
429 can be downloaded from the Argo Global Data Assembly Center  
430 (<ftp://ftp.ifremer.fr/ifremer/argo/>). These data were collected and made freely available by the  
431 International Argo Program and the national programs that contribute to it:  
432 (<http://www.argo.ucsd.edu>, <https://www.ocean-ops.org>). The Argo Program is part of the  
433 Global Ocean Observing System. We thank the Argo Data Management team (ADMT) and the  
434 BGC-Argo Data Management team (BGC ADMT). The specific float used in this study was  
435 funded by the ARC SRI for Antarctic Gateway Partnership (Project ID SR140300001). We  
436 thank the captain and crew of RV Investigator voyage IN2016\_V03 and chief scientist  
437 Bernadette Sloyan for deploying the float. Ssalto/Duacs altimeter product was produced and

438 distributed by the Copernicus Marine and Environment Monitoring Service (CMEMS,  
439 <https://marine.copernicus.eu/>). ERA5 wind speed and net heat flux reanalysis products were  
440 downloaded from <https://cds.climate.copernicus.eu/cdsapp#!/home>. Monthly GlobColour  
441 products were downloaded from CMEMS and MODIS products from the NASA Ocean Color  
442 website (<https://oceancolor.gsfc.nasa.gov>). The sea-ice product was downloaded from  
443 <https://nsidc.org/data/nsidc-0081>.

444

#### 445 **Author contributions**

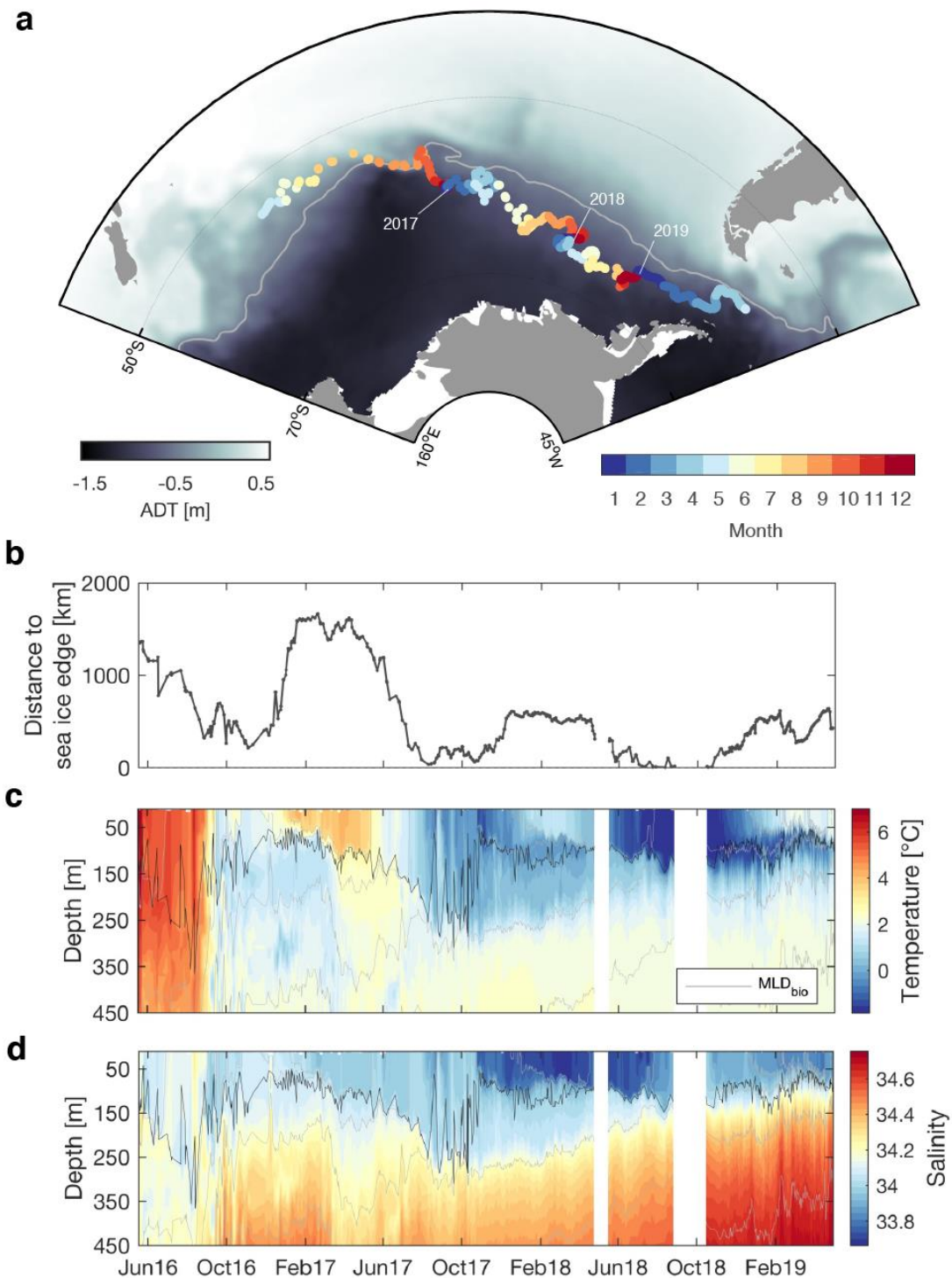
446 LL and JL designed the study and conducted the data analysis. LL wrote the manuscript. JL  
447 contributed to the data collection and to manuscript review and editing. NB conducted the mean  
448 particle diameter analysis and contributed to manuscript review and editing. PS and PWB  
449 contributed to the data collection and writing, and helped to design the study.

450

#### 451 **Competing financial interests**

452 The authors declare no competing financial interests.

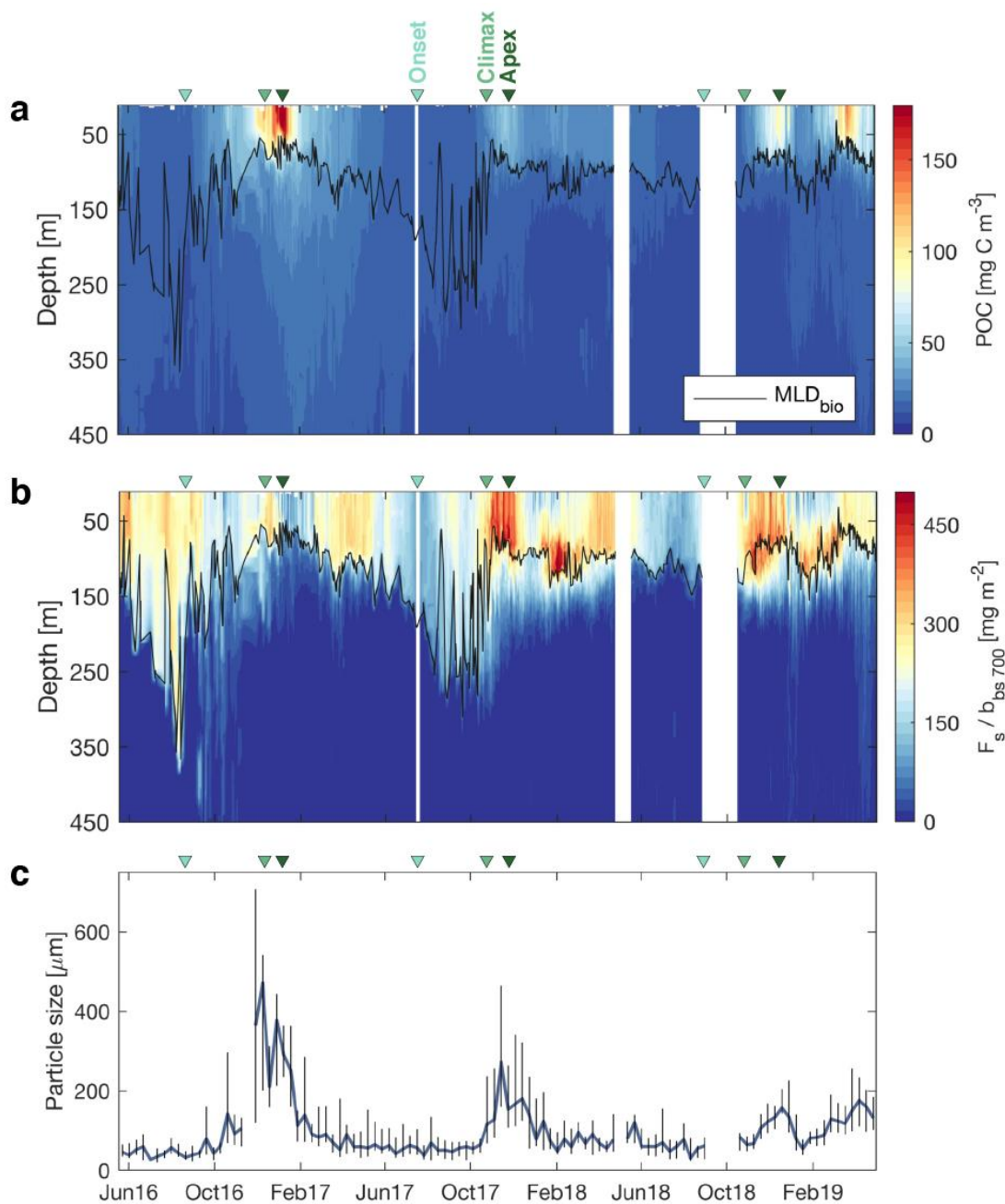
453



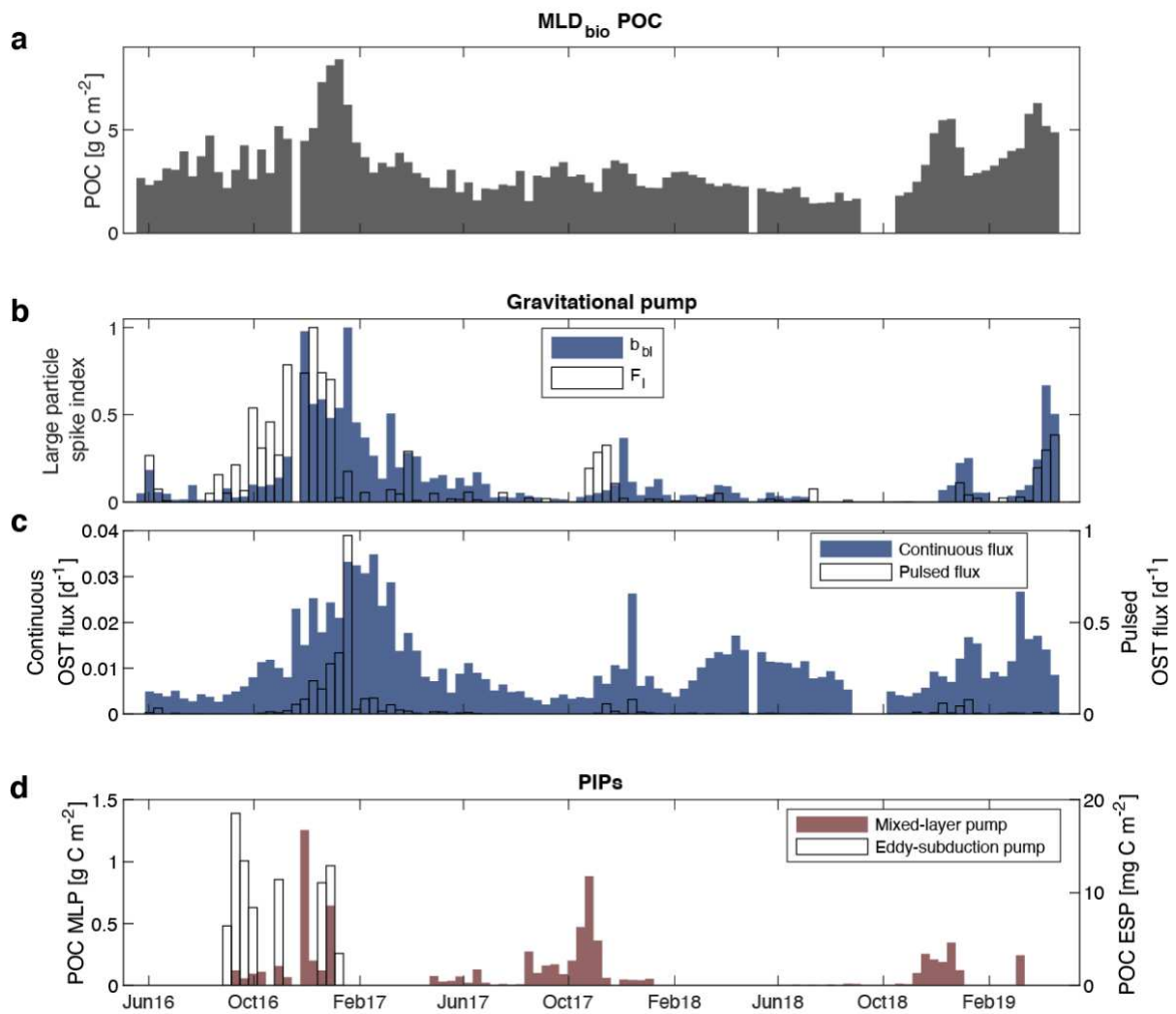
455

456 **Figure 1** Contrasting environmental conditions in the Pacific sector of the Southern Ocean. (a) Float  
 457 surfacing positions (every 1 to 5 days) during its 36-month mission. Background map is a climatology of Absolute  
 458 Dynamic Topography (ADT). Light grey line indicates the climatological position of the Polar Front (ADT=-0.48  
 459 m) used in Ardyna et al. (2017)<sup>66</sup> and derived from Swart et al. (2010)<sup>67</sup>. (b) Minimum distance between float  
 460 positions and the sea ice edge, defined as the 15% sea ice concentration limit. Vertical sections of (c) temperature

461 and (d) salinity recorded by the float. Light grey lines are isopycnals and the dark line is the mixing layer depth as  
 462 defined by biological criteria ( $MLD_{bio}$ , see Methods). Periods with missing data are blank in panels c and d.

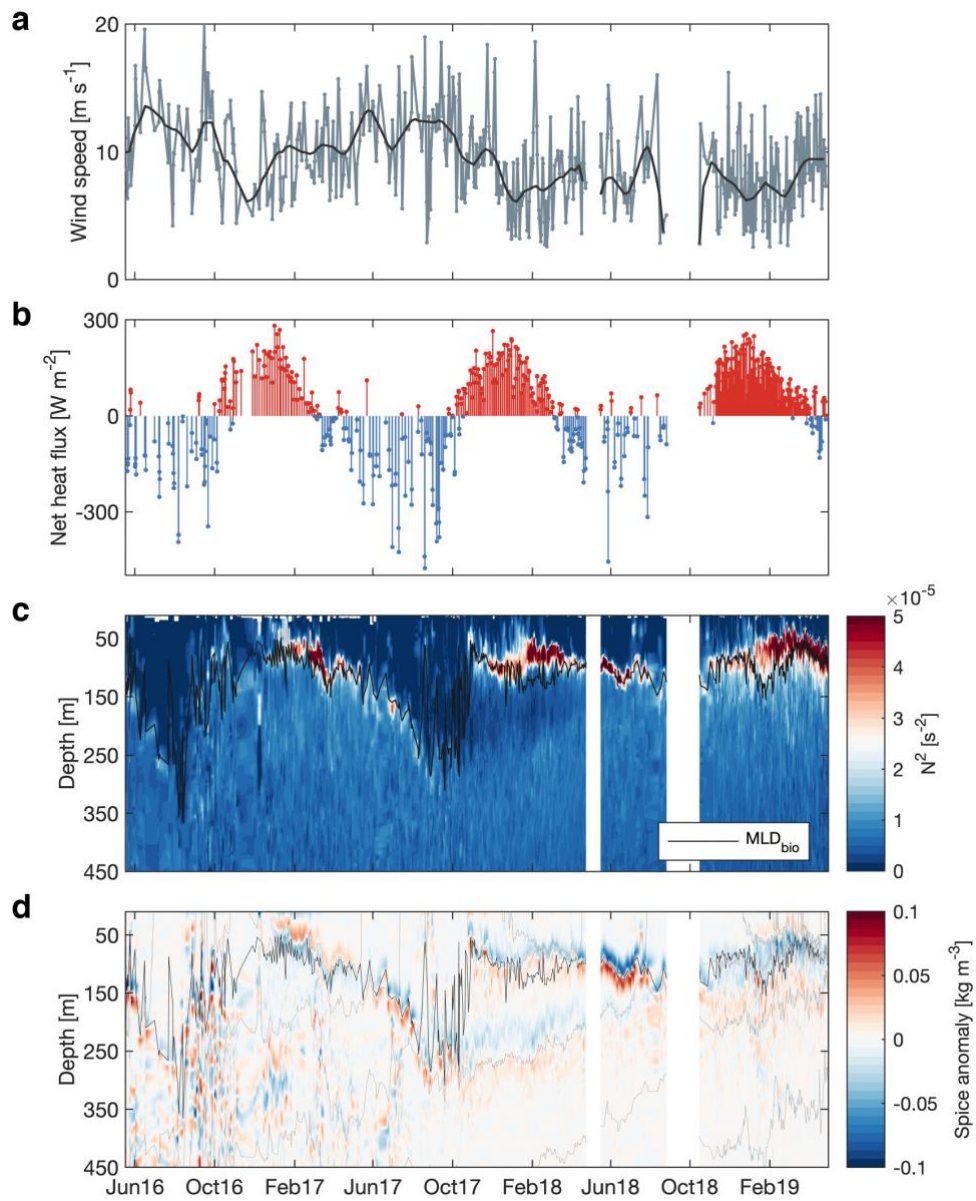


463  
 464 **Figure 2 Characteristics of the particle assemblage over three annual cycles evidenced by bio-optical**  
 465 **proxies.** Vertical sections of (a) particulate organic carbon (POC), and (b) chlorophyll fluorescence to  
 466 backscattering ratio  $F_s / b_{bs\ 700}$ . Black lines show the mixing layer depth ( $MLD_{bio}$ ). (c) Mean particle size (diameter)  
 467 in the upper 50 m. The blue line and vertical black lines represent the median and inter-quartile ranges,  
 468 respectively, over 10-day bins. As milestones, triangles on top of each panel mark the timing of onset (first positive  
 469 net phytoplankton accumulation), climax (maximum accumulation) and apex (maximum bulk phytoplankton  
 470 biomass) for each bloom, following the method in Uchida et al. 2019<sup>65</sup> (see Methods).



471  
472

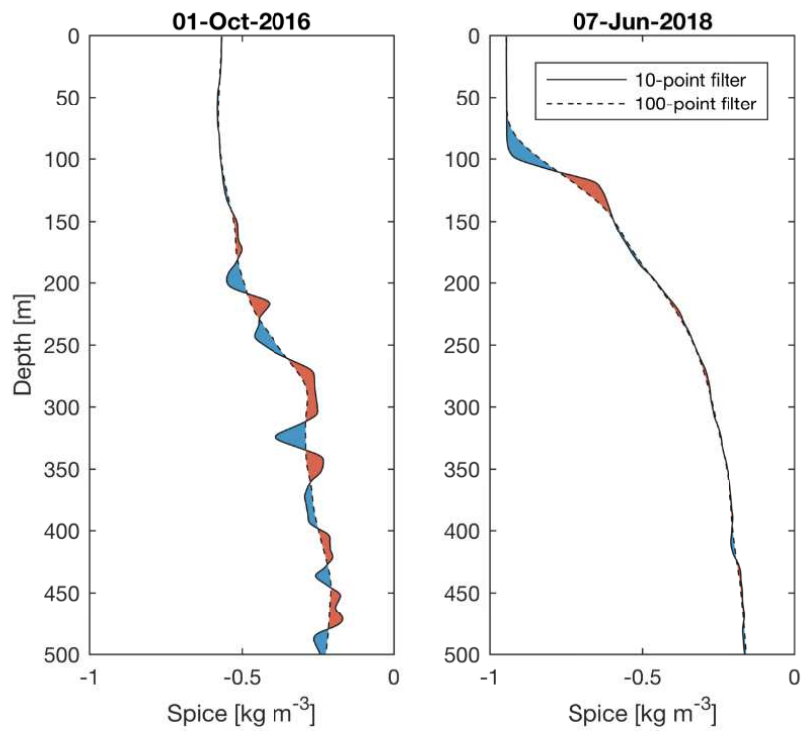
473 **Figure 3 Seasonality of multiple carbon export pathways.** (a) Stock of particulate organic carbon (POC) in  
 474 MLD<sub>bio</sub>. (b) Spike index calculated as depth-integrated  $b_{bl}$  and  $F_l$ , from MLD<sub>bio</sub> to 500 m, and normalised by  
 475 their minimum and maximum values (no units, see Methods). (c) Continuous and pulsed flux measured by the  
 476 optical sediment trap (OST) at ~300 m. Pulsed flux is defined as discontinuities in the OST record (see Methods).  
 477 Panels b and c show two complementary approaches to characterise the BGP. (d) Green empty bars show the stock  
 478 of POC in subsurface layers presenting anomalous POC, Apparent Oxygen Utilization (AOU) and spice, related  
 479 to ESP events. Brown bars show the stock of POC in the remnant layer, associated with MLP events. In all panels,  
 480 data has been averaged over 10-day bins. For the ESP and MLP, this averaging avoids double counting POC stocks  
 481 for events sampled multiple times.



483

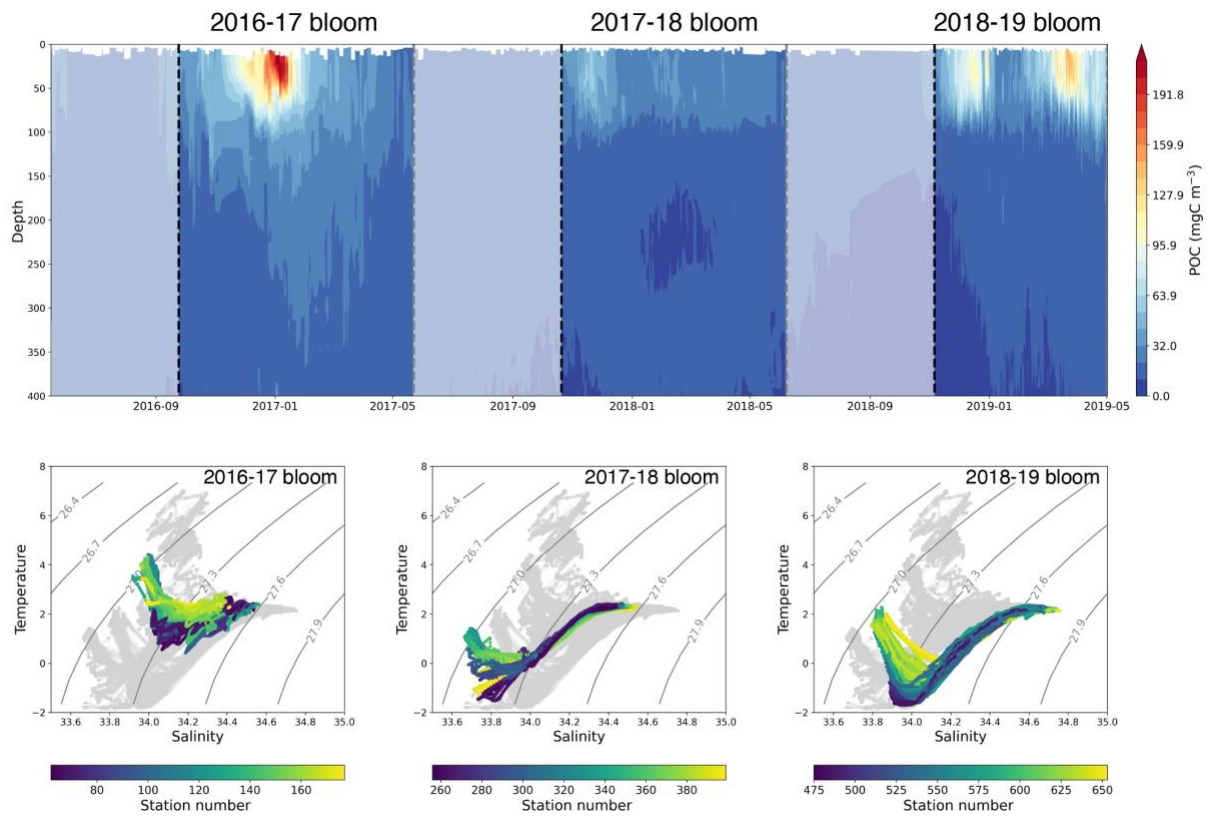
484 **Figure S1 Environmental factors controlling phytoplankton phenology and vertical carbon export.** (a) Daily  
 485 wind speed at 10 m above the ocean surface, along the float trajectory. The black line is a 30-day smooth. (b) Daily  
 486 net heat flux along the float trajectory, with positive values referring to a flux from the atmosphere to the ocean.  
 487 Vertical sections of (c) Buoyancy frequency  $N^2$  and (d) spice anomaly (see Fig S2) recorded by the float.

488



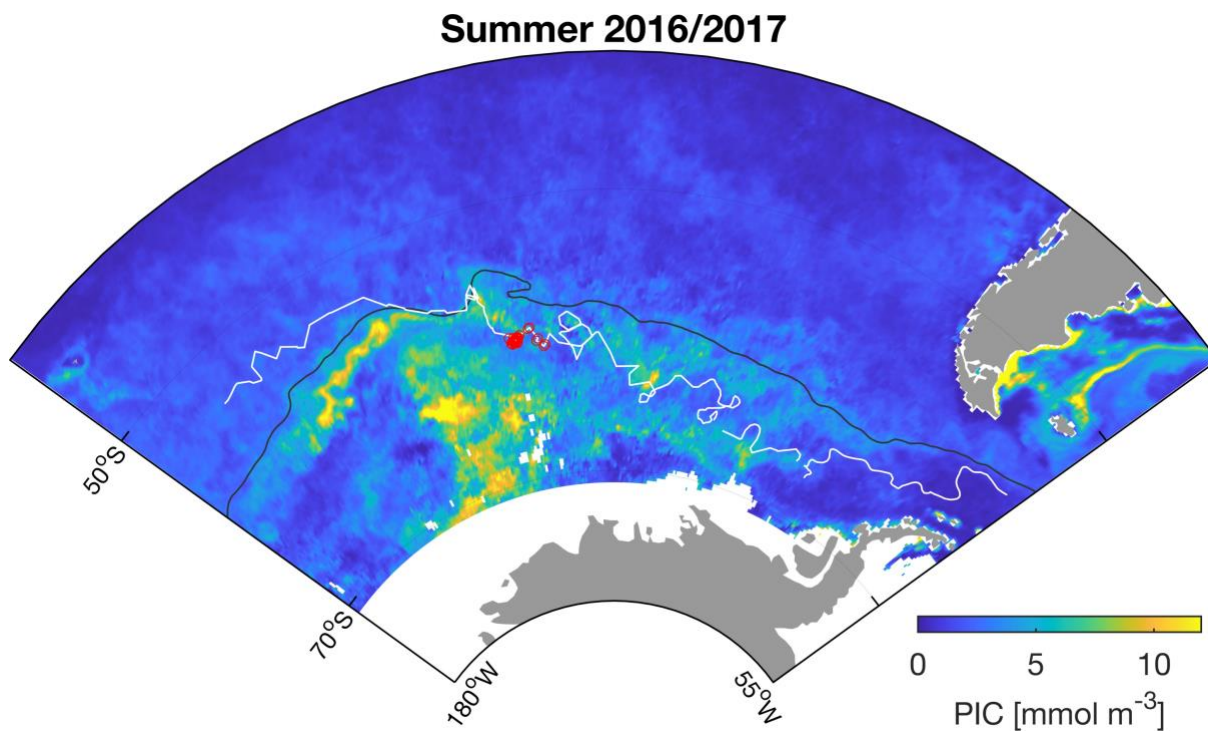
489

490 **Figure S2 Spice anomaly reveals the interleaving of water masses.** Examples of spice profile on October 1<sup>st</sup>  
 491 2016 (left), when the float crossed the polar front, and June 7<sup>th</sup> 2018 (right), when a strong dipole in the spice  
 492 anomaly was observed at the base of the melt-water layer (see Fig. 1d). Dashed and continuous black lines show  
 493 a 100-point (or 100 m) and 10-point (or 10 m) moving average of spice profiles, respectively. Red and blue shaded  
 494 areas indicate positive and negative spice anomaly (difference between 10- and 100-point filtered signals),  
 495 respectively, as shown on Fig. S1d.



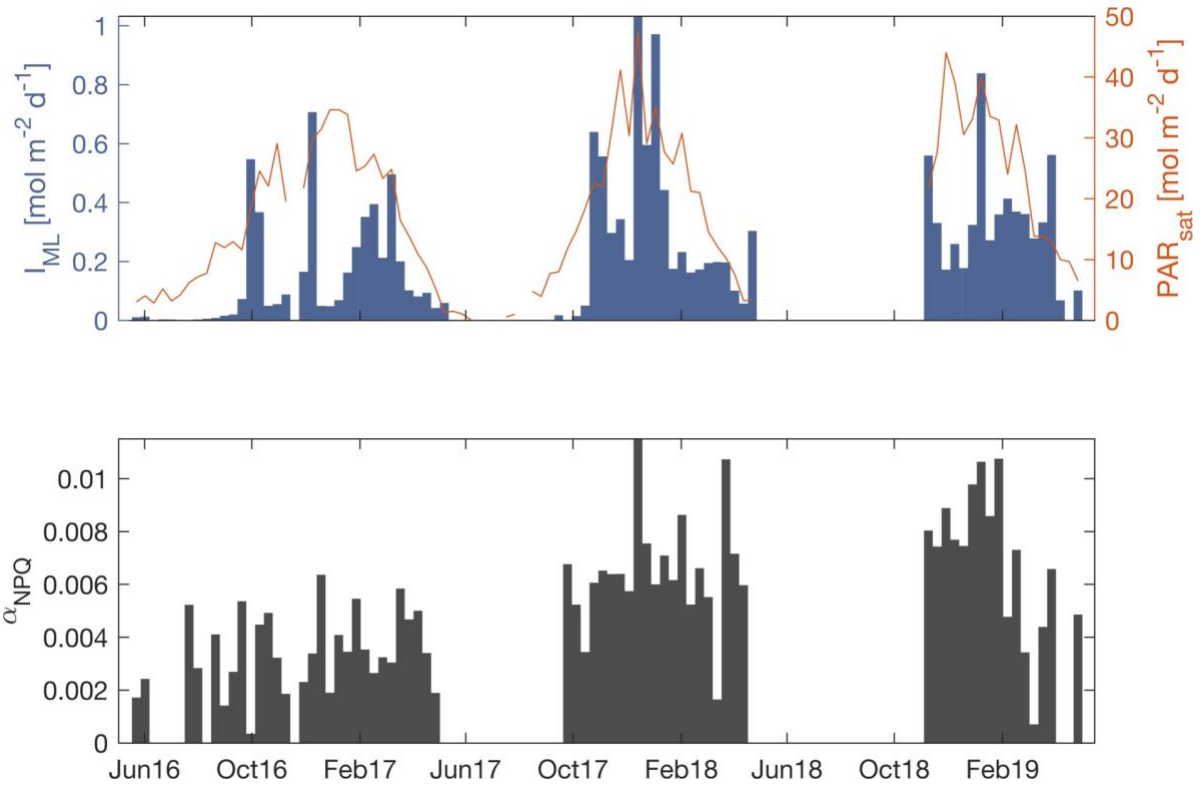
496

497 **Figure S3 Pseudo-Lagrangian framework.** The float temporal section was divided into three periods in which  
 498 the contiguous nature of the water masses was verified (areas delimited by vertical dashed lines in top panel). The  
 499 three TS diagrams at the bottom reveal that the float did not cross any strong water mass boundaries during each  
 500 period of interest. Grey dots in the background show data points of the complete timeseries.



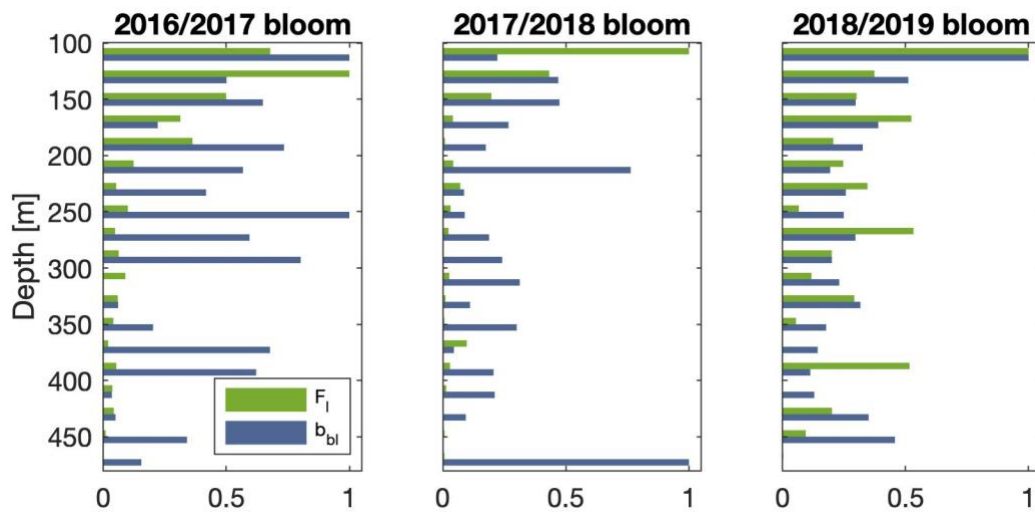
502 **Figure S4 Satellite Particulate Inorganic Carbon (PIC) reveals the presence of a coccolithophore bloom in**  
 503 **austral summer 2016-17.** Trajectory of the float superimposed on summer (December 2016 to February 2017)  
 504 composite GlobColour image (25 km) of PIC. Red circles indicate the location of the summer float profiles where  
 505 we observed a strong decrease in the  $F_s / b_{bs}$  ratio.

506



507

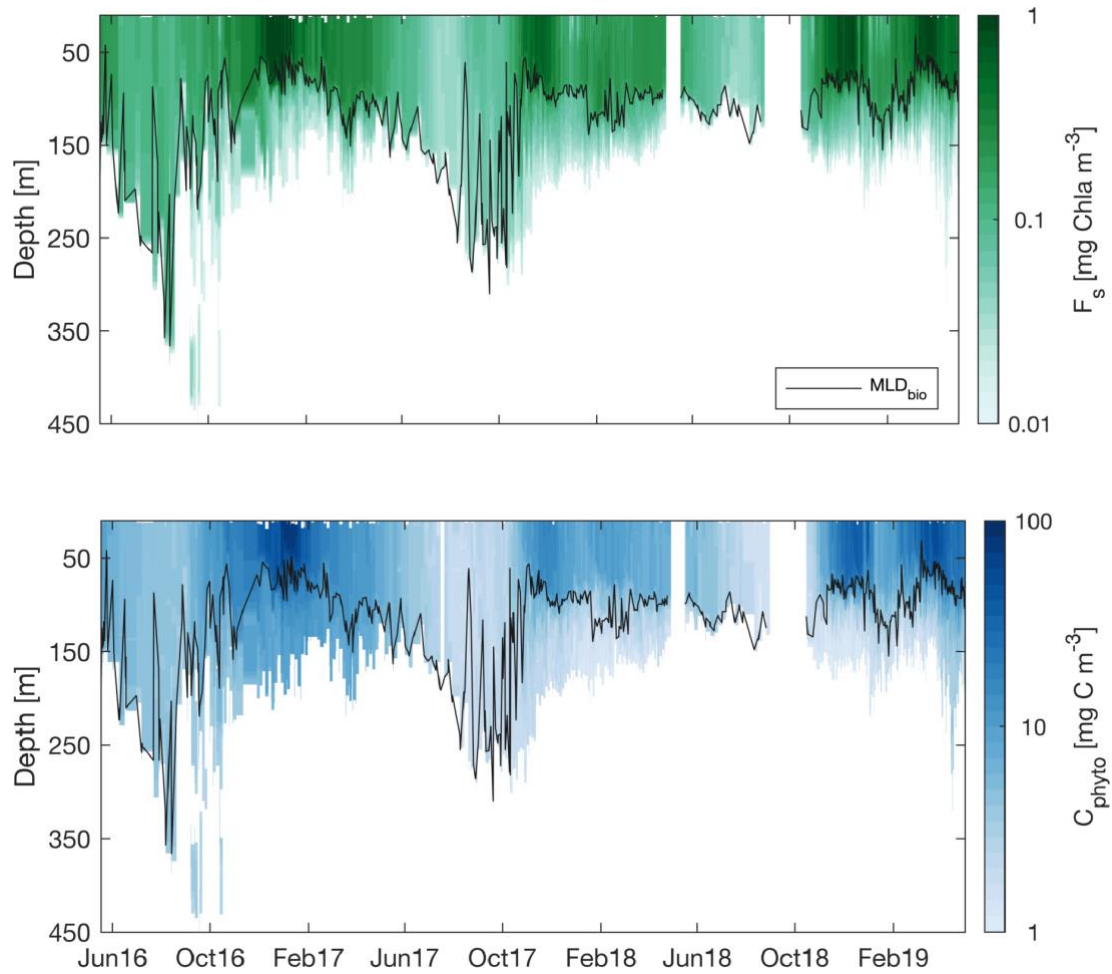
508 **Figure S5 Iron and light limitation play a key role in shaping phytoplankton phenology in the SO.** Top  
 509 panel, median light level within the mixing layer ( $I_{ML}$ , blue bars) derived from satellite daily mean PAR (red  
 510 curve).  $I_{ML}$  is an indicator of the light history of phytoplankton cells and has been previously used as a descriptor  
 511 of photoacclimation<sup>59</sup>. Gaps in the timeseries are due to the winter polar night or the presence of sea ice. Bottom  
 512 panel, initial slope of the non-photochemical quenching (NPQ) versus instantaneous iPAR curve ( $\alpha_{\text{NPQ}}$ ).  $\alpha_{\text{NPQ}}$  is a  
 513 proxy for phytoplankton iron limitation<sup>55</sup>, the higher  $\alpha_{\text{NPQ}}$ , the more iron-limited.



514

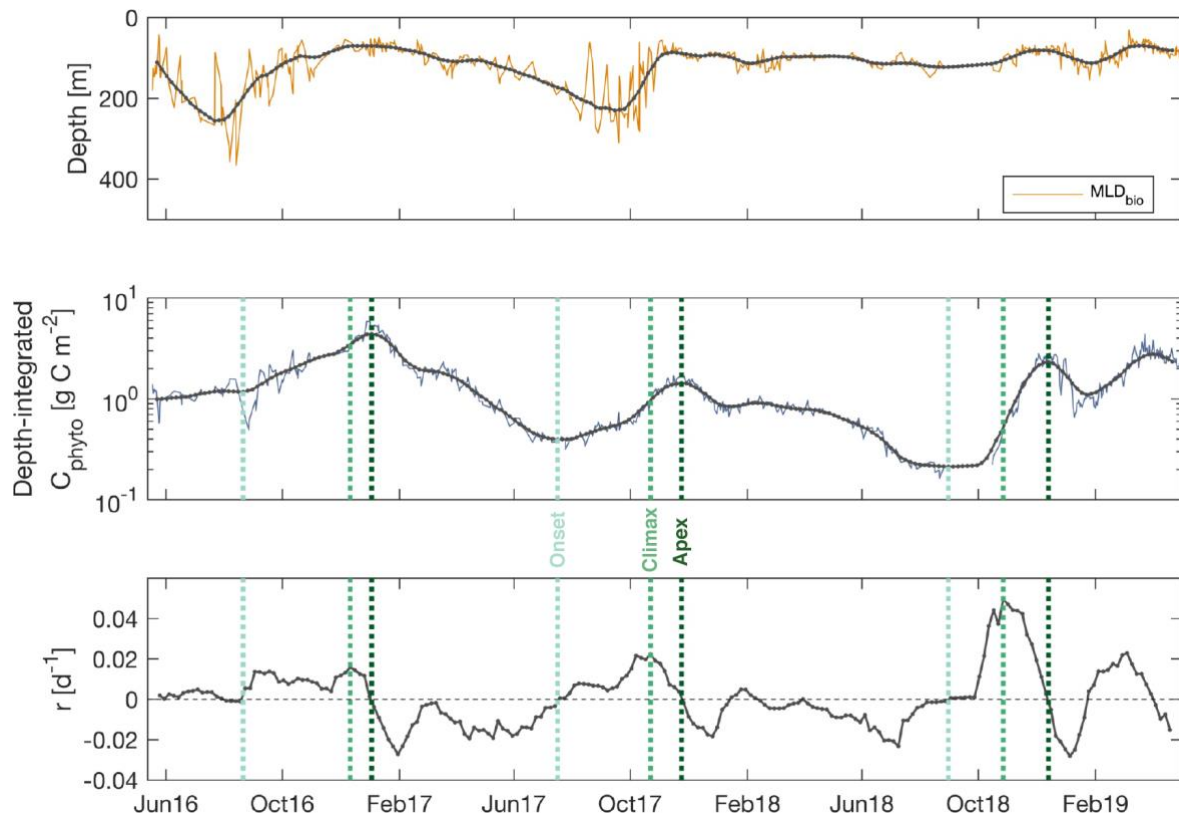
515 **Figure S6 Vertical distribution of  $F_1$  and  $b_{bl}$** , summed in 20 m bins over the course of the blooming period (from  
 516 climax to 30 days after apex for the first two blooms and from climax to the end of the timeseries for the last bloom  
 517 which shows two distinct biomass peaks few months apart, see Fig. S8) and normalised by their minimum and  
 518 maximum values. As opposed to  $b_{bl}$ ,  $F_1$  was quickly attenuated with depth, although this is less clear for the last  
 519 2018-19 bloom.

520



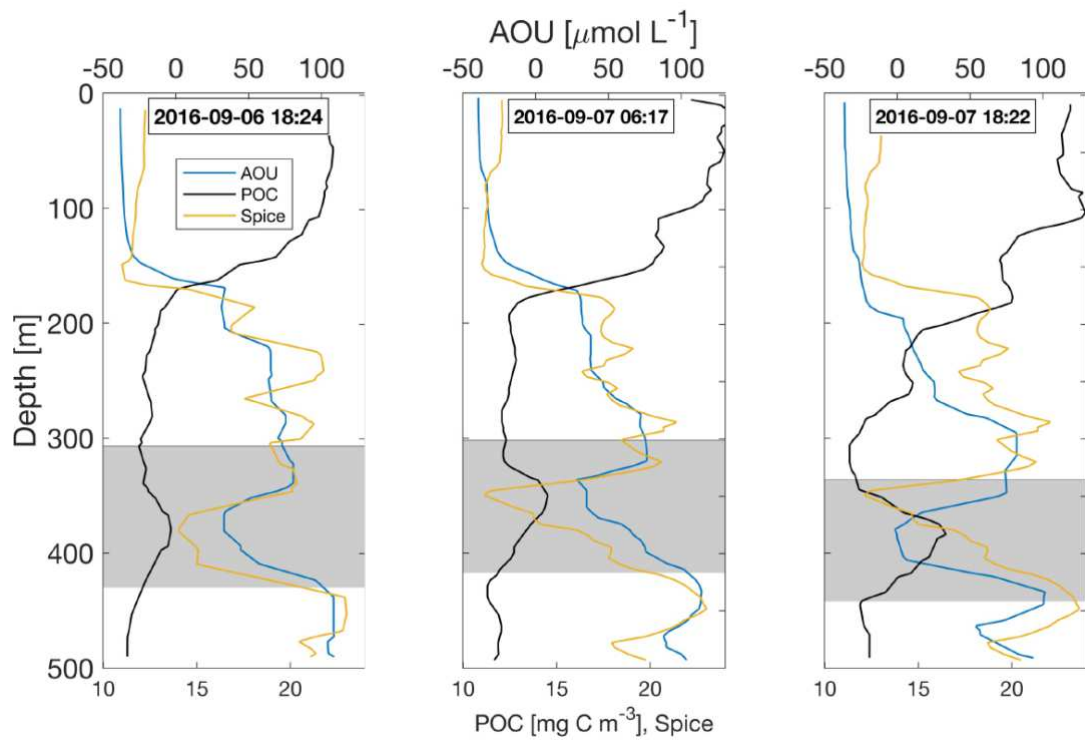
521

522 **Figure S7 Bulk phytoplankton biomass derived from optical measurements.** Vertical sections of Chlorophyll  
 523 *a* fluorescence ( $F_s$ , top), and phytoplankton carbon ( $C_{\text{phyto}}$ ) derived from the backscattering at 470 nm ( $b_{\text{bp } 470}$ ,  
 524 bottom). Both colour bars are on a log scale. Black lines show the mixing layer depth. In the bottom panel,  $C_{\text{phyto}}$   
 525 was masked out where  $F_s \leq 0$ . The bulk phytoplankton biomass was then calculated by vertically integrating  
 526 masked  $C_{\text{phyto}}$  over the whole water column, following Uchida et al. (2019)<sup>65</sup>. Note that SCMs are barely discernible  
 527 in the top figure due to the use of running minimum and maximum filters to compute  $F_s$ , which partially erases  
 528 subsurface peaks in fluorescence (see Methods).



529

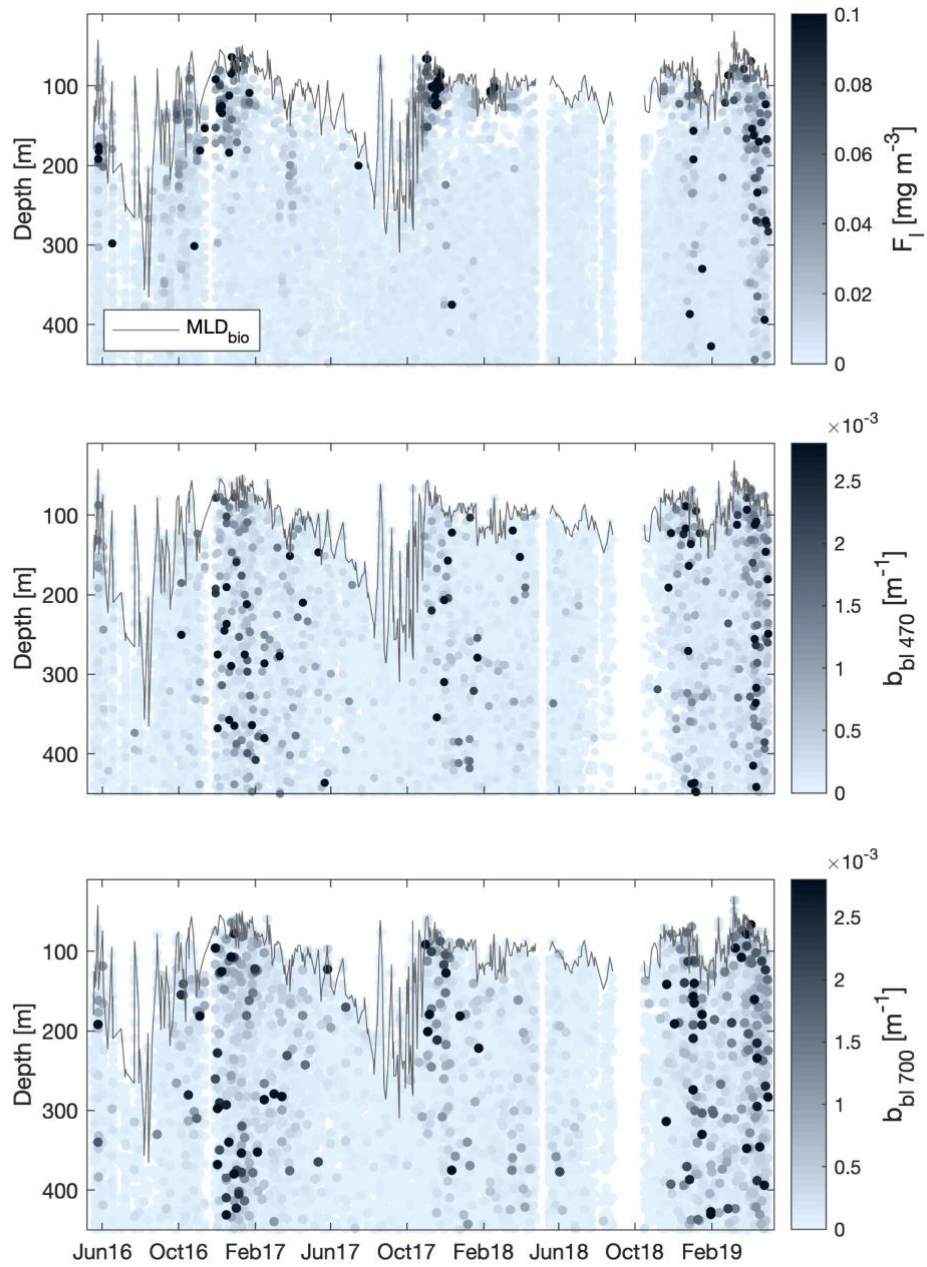
530 **Figure S8 Phytoplankton phenology metrics.** Top, mixing layer depth ( $MLD_{bio}$ ). Middle, bulk phytoplankton  
 531 biomass. Continuous black lines in the top two panels show 30-day moving averages of these variables. Bottom,  
 532 net growth rate  $r$  calculated from smoothed depth-integrated  $C_{phyto}$  (see Methods). Vertical dotted green lines  
 533 indicate the timing of onset, climax and apex of the three phytoplankton blooms recorded by the float.



534

535 **Figure S9 Examples of ESP signatures** identified from three consecutive AOU, POC and spice profiles in early  
 536 September 2016. Shaded grey areas highlight features falling within the same water mass (defined by a potential  
 537 density of  $27.31 \pm 0.04 \text{ kg m}^{-3}$ ).

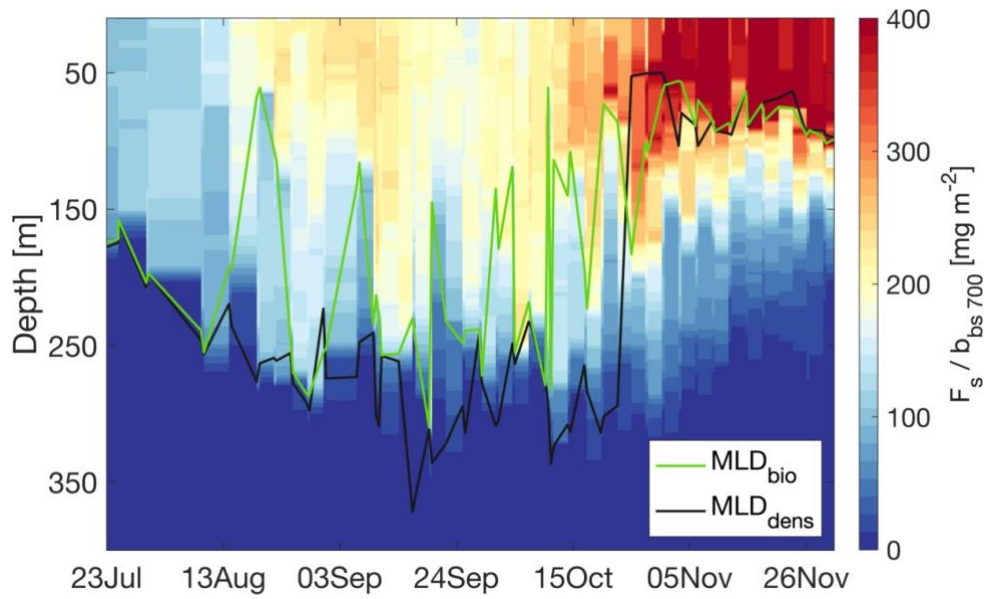
538



539

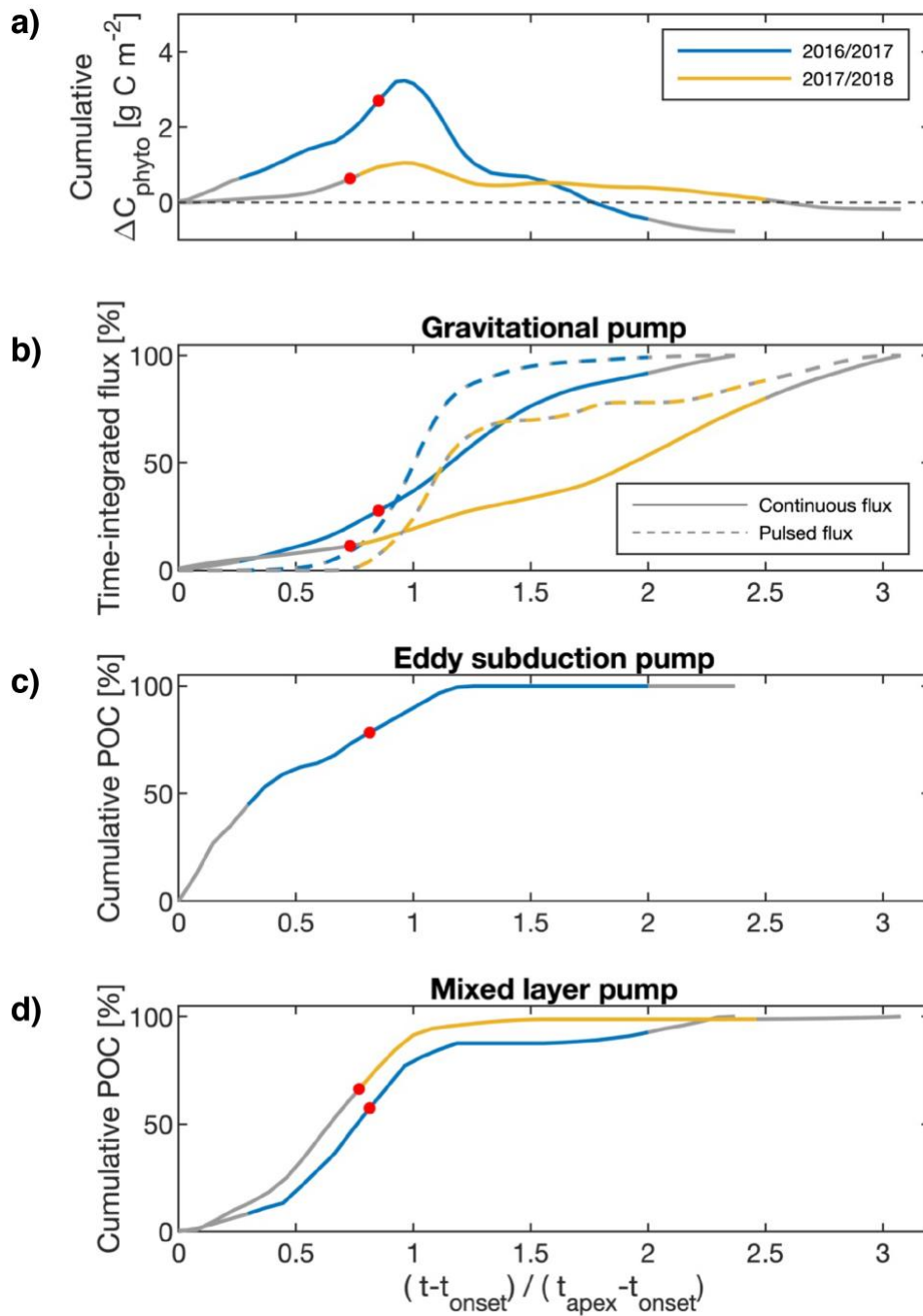
540 **Figure S10** Sections of large-particle fluorescence  $F_l$  (top), revealing the presence of fresh phytoplankton  
 541 aggregates, and large-particle backscattering  $b_{bl\ 470}$  (middle) and  $b_{bl\ 700}$  (bottom), which additionally include fecal  
 542 and detrital matter.

543



544

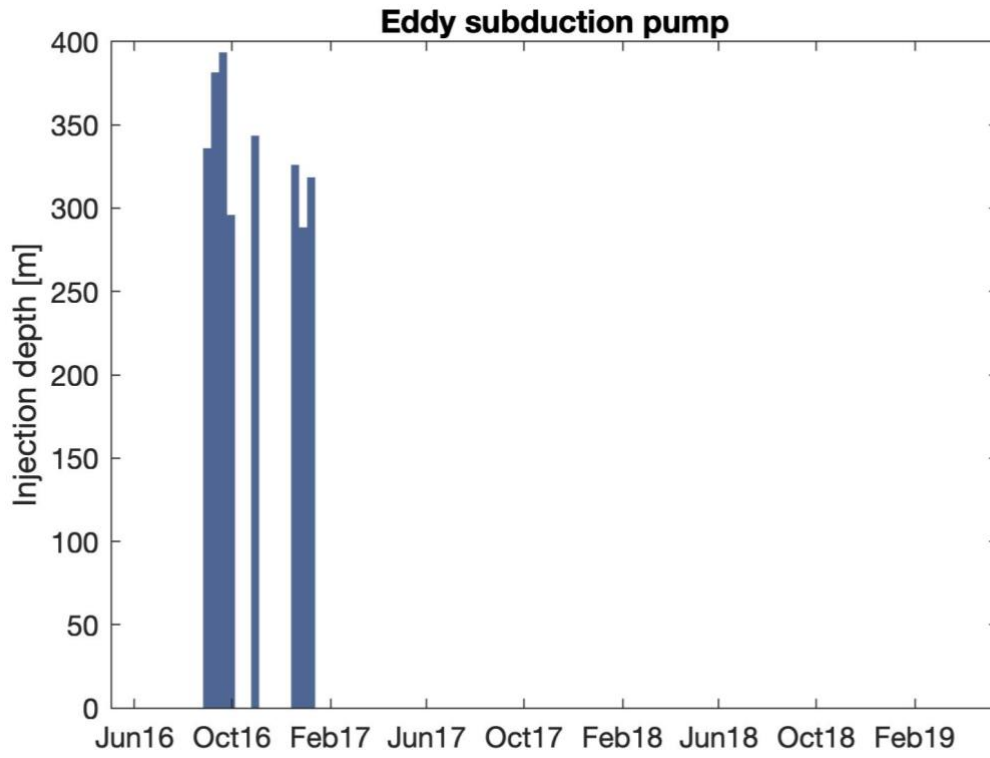
545 **Figure S11 Illustration of the MLP during the 2017-18 bloom** which shows how rapid and intermittent re-  
 546 stratifications of the mixing layer isolates fresh particles at depth. The freshness of particles is revealed by the  
 547 relatively high  $F_s / b_{bs}$  ratio (100-200  $\text{mg m}^{-2}$ ) observed in the remnant layer (delimited by  $\text{MLD}_{\text{bio}}$  at the top and  
 548  $\text{MLD}_{\text{dens}}$  at the bottom).



550

551 **Figure S12 Relationship between phytoplankton phenology and carbon export pathways.** a) cumulative sum  
 552 of  $\Delta C_{\text{phyto}}$ , the temporal difference of bulk phytoplankton biomass. b) Time-integrated continuous (solid lines) and  
 553 pulsed flux (dashed lines) estimated from optical sediment trap (OST) measurements. c) Cumulative POC stock  
 554 in eddy-induced subsurface anomalies, and d) MLP remnant layers. POC stocks were first averaged over 10 days,  
 555 as shown in Fig. 3, to avoid double counting when the float samples the same event multiple times. Each colour  
 556 represents a different seasonal cycle. The coloured part of the curves indicates the region where we assumed a  
 557 quasi-Lagrangian framework (See Fig. S3 and Methods). Red dots mark the timing of the bloom climax. The time  
 558 axis was rescaled by the onset ( $t_{\text{onset}}$ ) and the apex ( $t_{\text{apex}}$ ) of the bloom, so that 0 corresponds to the onset and 1 to

559 the apex. Note that the last seasonal cycle (2018/2019) is not represented due to missing data early in the productive  
560 season.  
561



562

563 **Figure S13** Mean depths of the detected subsurface anomalies related to ESP events.

## 564 **References**

- 565 1. Schlitzer, R. Carbon export fluxes in the Southern Ocean: results from inverse modeling and comparison with  
566 satellite-based estimates. *Deep Sea Res. Part II Top. Stud. Oceanogr.* **49**, 1623–1644 (2002).
- 567 2. Volk, T. & Hoffert, M. I. Ocean carbon pumps: Analysis of relative strengths and efficiencies in ocean-driven  
568 atmospheric CO<sub>2</sub> changes. in 99–110 (American Geophysical Union, 1985). doi:10.1029/GM032p0099
- 569 3. Boyd, P. W., Claustre, H., Levy, M., Siegel, D. A. & Weber, T. Multi-faceted particle pumps drive carbon  
570 sequestration in the ocean. *Nature* **568**, 327–335 (2019).
- 571 4. Burd, A. B. *et al.* Assessing the apparent imbalance between geochemical and biochemical indicators of meso- and  
572 bathypelagic biological activity: What the @\$#! is wrong with present calculations of carbon budgets? *Deep. Res.*  
573 *Part II Top. Stud. Oceanogr.* **57**, 1557–1571 (2010).
- 574 5. Omand, M. M. *et al.* Eddy-driven subduction exports particulate organic carbon from the spring bloom. *Science (80-*  
575 *).* **348**, 222–225 (2015).
- 576 6. Llorc, J. *et al.* Evaluating Southern Ocean Carbon Eddy-Pump From Biogeochemical-Argo Floats. *J. Geophys. Res.*  
577 *Ocean.* **123**, 971–984 (2018).
- 578 7. Stukel, M. R. & Ducklow, H. W. Stirring Up the Biological Pump: Vertical Mixing and Carbon Export in the  
579 Southern Ocean. *Global Biogeochem. Cycles* **31**, 1420–1434 (2017).
- 580 8. Lacour, L., Briggs, N., Claustre, H., Ardyna, M. & Dall’Olmo, G. The Intraseasonal Dynamics of the Mixed Layer  
581 Pump in the Subpolar North Atlantic Ocean: A Biogeochemical-Argo Float Approach. *Global Biogeochem. Cycles*  
582 **33**, 266–281 (2019).
- 583 9. Dall’Olmo, G., Dingle, J., Polimene, L., Brewin, R. J. W. & Claustre, H. Substantial energy input to the mesopelagic  
584 ecosystem from the seasonal mixed-layer pump. *Nat. Geosci.* (2016). doi:10.1038/ngeo2818
- 585 10. Stukel, M. R., Song, H., Goericke, R. & Miller, A. J. The role of subduction and gravitational sinking in particle  
586 export, carbon sequestration, and the remineralization length scale in the California Current Ecosystem. *Limnol.*  
587 *Oceanogr.* **63**, 363–383 (2018).
- 588 11. Resplandy, L., Lévy, M. & McGillicuddy Jr, D. J. Effects of eddy-driven subduction on ocean biological carbon  
589 pump. *Global Biogeochem. Cycles* (2019). doi:10.1029/2018GB006125
- 590 12. Irigoien, X. *et al.* Large mesopelagic fishes biomass and trophic efficiency in the open ocean. *Nat. Commun.* **5**,  
591 (2014).
- 592 13. Jónasdóttir, S. H., Visser, A. W., Richardson, K. & Heath, M. R. Seasonal copepod lipid pump promotes carbon  
593 sequestration in the deep North Atlantic. *Proc. Natl. Acad. Sci.* **112**, 12122–12126 (2015).
- 594 14. Levy, M. *et al.* Physical pathways for carbon transfers between the surface mixed layer and the ocean interior.  
595 *Global Biogeochem. Cycles* **27**, 1001–1012 (2013).
- 596 15. Estapa, M. L., Feen, M. L. & Breves, E. Direct Observations of Biological Carbon Export From Profiling Floats in  
597 the Subtropical North Atlantic. *Global Biogeochem. Cycles* **33**, 282–300 (2019).

- 598 16. Bishop, J. K. B. & Wood, T. J. Year-round observations of carbon biomass and flux variability in the Southern  
599 Ocean. *Global Biogeochem. Cycles* **23**, (2009).
- 600 17. Lacour, L., Briggs, N., Claustre, H., Ardyna, M. & Dall’Olmo, G. The Intraseasonal Dynamics of the Mixed Layer  
601 Pump in the Subpolar North Atlantic Ocean: A Biogeochemical-Argo Float Approach. *Global Biogeochem. Cycles*  
602 **33**, 266–281 (2019).
- 603 18. Briggs, N. *et al.* High-resolution observations of aggregate flux during a sub-polar North Atlantic spring bloom.  
604 *Deep Sea Res. Part I Oceanogr. Res. Pap.* **58**, 1031–1039 (2011).
- 605 19. Estapa, M., Durkin, C., Buesseler, K., Johnson, R. & Feen, M. Carbon flux from bio-optical profiling floats:  
606 Calibrating transmissometers for use as optical sediment traps. *Deep. Res. Part I Oceanogr. Res. Pap.* **120**, 100–111  
607 (2017).
- 608 20. Cetinić, I. *et al.* A simple optical index shows spatial and temporal heterogeneity in phytoplankton community  
609 composition during the 2008 North Atlantic Bloom Experiment. *Biogeosciences* **12**, 2179–2194 (2015).
- 610 21. Rembauville, M. *et al.* Plankton Assemblage Estimated With BGC-Argo Floats in the Southern Ocean: Implications  
611 for Seasonal Successions and Particle Export. *J. Geophys. Res. Ocean.* (2017). doi:10.1002/2017JC013067
- 612 22. Geider, R. J. Light and Temperature Dependence of the Carbon to Chlorophyll a Ratio in Microalgae and  
613 Cyanobacteria: Implications for Physiology and Growth of Phytoplankton. *New Phytol.* **106**, 1–34 (1987).
- 614 23. Terrats, L., Claustre, H., Cornec, M., Mangin, A. & Neukermans, G. Detection of Coccolithophore Blooms With  
615 BioGeoChemical-Argo Floats. *Geophys. Res. Lett.* **47**, e2020GL090559 (2020).
- 616 24. Balch, W. M. *et al.* The contribution of coccolithophores to the optical and inorganic carbon budgets during the  
617 Southern Ocean Gas Exchange Experiment: New evidence in support of the Great Calcite Belt hypothesis. *J.*  
618 *Geophys. Res. Ocean.* **116**, 1–14 (2011).
- 619 25. Balch, W. M., Gordon, H. R., Bowler, B. C., Drapeau, D. T. & Booth, E. S. Calcium carbonate measurements in the  
620 surface global ocean based on Moderate-Resolution Imaging Spectroradiometer data. *J. Geophys. Res. C Ocean.*  
621 **110**, 1–21 (2005).
- 622 26. Klaas, C. & Archer, D. E. Association of sinking organic matter with various types of mineral ballast in the deep  
623 sea: Implications for the rain ratio. *Global Biogeochem. Cycles* **16**, 63-1-63–14 (2002).
- 624 27. Ryan-Keogh, T. J. & Smith, W. O. Temporal patterns of iron limitation in the Ross Sea as determined from  
625 chlorophyll fluorescence. *J. Mar. Syst.* **215**, 103500 (2021).
- 626 28. Sedwick, P. N., Di Tullio, G. R. & Mackey, D. J. Iron and manganese in the Ross Sea, Seasonal iron limitation in  
627 Antarctic. *J. Geophys. Res. Ocean.* **105**, 11321–11336 (2000).
- 628 29. Hopkinson, B. M. *et al.* Iron limitation across chlorophyll gradients in the southern Drake Passage: Phytoplankton  
629 responses to iron addition and photosynthetic indicators of iron stress. *Limnol. Oceanogr.* **52**, 2540–2554 (2007).
- 630 30. Litchman, E. Resource Competition and the Ecological Success of Phytoplankton. *Evolution of Primary Producers*  
631 *in the Sea* 351–375 (2007). doi:10.1016/B978-012370518-1/50017-5
- 632 31. Rembauville, M., Blain, S., Armand, L., Quéguiner, B. & Salter, I. Export fluxes in a naturally iron-fertilized area of

- 633 the Southern Ocean - Part 2: Importance of diatom resting spores and faecal pellets for export. *Biogeosciences* **12**,  
634 3171–3195 (2015).
- 635 32. Riebesell, U. *et al.* Competitive fitness of a predominant pelagic calcifier impaired by ocean acidification. *Nat.*  
636 *Geosci.* **10**, 19–23 (2017).
- 637 33. Blain, S., Rembauville, M., Crispi, O. & Obernosterer, I. Synchronized autonomous sampling reveals coupled pulses  
638 of biomass and export of morphologically different diatoms in the Southern Ocean. *Limnol. Oceanogr.* **66**, 753–764  
639 (2021).
- 640 34. Estapa, M. L., Buesseler, K., Boss, E. & Gerbi, G. Autonomous, high-resolution observations of particle flux in the  
641 oligotrophic ocean. *Biogeosciences Discuss.* **10**, 1229–1265 (2013).
- 642 35. Dall’Olmo, G. & Mork, K. A. Carbon export by small particles in the Norwegian Sea. *Geophys. Res. Lett.* **41**, 2921–  
643 2927 (2014).
- 644 36. Dever, M., Nicholson, D., Omand, M. M. & Mahadevan, A. Size-Differentiated Export Flux in Different Dynamical  
645 Regimes in the Ocean. *Global Biogeochem. Cycles* **35**, 1–20 (2021).
- 646 37. D’Asaro, E. Convection and the seeding of the North Atlantic bloom. *J. Mar. Syst.* **69**, 233–237 (2008).
- 647 38. Spall, M. A. Frontogenesis, subduction, and cross-front exchange at upper ocean fronts. *J. Geophys. Res.* **100**, 2543  
648 (1995).
- 649 39. Asper, V. L. & Smith, W. O. Abundance, distribution and sinking rates of aggregates in the Ross Sea, Antarctica.  
650 *Deep. Res. Part I Oceanogr. Res. Pap.* **50**, 131–150 (2003).
- 651 40. Wong, A., Keeley, R., Carval, T. & Argo Data Management Team. Argo Quality Control Manual For CTD and  
652 Trajectory Data. 1–58 (2020).
- 653 41. Schmechtig, C. *et al.* *Processing Bio-Argo particle backscattering at the DAC level.* (Ifremer, 2018).  
654 doi:10.13155/39459
- 655 42. Schmechtig, C., Poteau, A., Claustre, H., D’Ortenzio, F. & Boss, E. *Processing bio-Argo chlorophyll-A*  
656 *concentration at the DAC level.* (Ifremer, 2015). doi:10.13155/39468
- 657 43. Schmechtig, C., Thierry, V. & The Bio-Argo Team. Argo Quality Control Manual for Biogeochemical Data. *Argo*  
658 *Data Manag.* 1–54 (2016).
- 659 44. Xing, X. *et al.* Improved correction for non-photochemical quenching of in situ chlorophyll fluorescence based on a  
660 synchronous irradiance profile. *Opt. Express* **26**, 24734–24751 (2018).
- 661 45. Johnson, K. S. *et al.* Air Oxygen Calibration of Oxygen Optodes on a Profiling Float Array. *J. Atmos. Ocean.*  
662 *Technol.* **32**, 2160–2172 (2015).
- 663 46. Johnson, K. S. *et al.* Biogeochemical sensor performance in the SOCCOM profiling float array. *J. Geophys. Res.*  
664 *Ocean.* (2017). doi:10.1002/2017JC012838
- 665 47. Graff, J. R. *et al.* Analytical phytoplankton carbon measurements spanning diverse ecosystems. *Deep Sea Res. Part I*  
666 *Oceanogr. Res. Pap.* **102**, 16–25 (2015).

- 667 48. Moreau, S., Boyd, P. W. & Strutton, P. G. Remote assessment of the fate of phytoplankton in the Southern Ocean  
668 sea-ice zone. *Nat. Commun.* **11**, 3108 (2020).
- 669 49. Mignot, A., Ferrari, R. & Claustre, H. Floats with bio-optical sensors reveal what processes trigger the North  
670 Atlantic bloom. *Nat. Commun.* **9**, 190 (2018).
- 671 50. Johnson, K. S., Plant, J. N., Dunne, J. P., Talley, L. D. & Sarmiento, J. L. Annual nitrate drawdown observed by  
672 SOCCOM profiling floats and the relationship to annual net community production. *J. Geophys. Res. Ocean.* **122**,  
673 6668–6683 (2017).
- 674 51. Briggs, N. T., Slade, W. H., Boss, E. & Perry, M. J. Method for estimating mean particle size from high-frequency  
675 fluctuations in beam attenuation or scattering measurements. *Appl. Opt.* **52**, 6710–25 (2013).
- 676 52. Bohren, C. F. & Huffman, D. R. *In Absorption and Scattering of Light by Small Particles*. (eds C.F. Bohren and  
677 D.R. Huffman, 1998).
- 678 53. Briggs, N., Dall’Olmo, G. & Claustre, H. Major role of particle fragmentation in regulating biological sequestration  
679 of CO<sub>2</sub> by the oceans. *Science (80-. )*. **367**, 791–793 (2020).
- 680 54. Huisman, J., Oostveen, P. van & Weissing, F. J. Critical Depth and Critical Turbulence: Two Different Mechanisms  
681 for the Development of Phytoplankton Blooms. *Limnol. Oceanogr.* **44**, 1781–1787 (1999).
- 682 55. Ryan-Keogh, T. J. & Thomalla, S. J. Deriving a Proxy for Iron Limitation From Chlorophyll Fluorescence on  
683 Buoyancy Gliders. *Front. Mar. Sci.* **7**, 1–13 (2020).
- 684 56. Schallenberg, C. *et al.* Diel quenching of Southern Ocean phytoplankton fluorescence is related to iron limitation.  
685 *Biogeosciences* **17**, 793–812 (2020).
- 686 57. Kropuenske, L. R. *et al.* Photophysiology in two major Southern Ocean phytoplankton taxa: Photoprotection in  
687 *Phaeocystis antarctica* and *Fragilariopsis cylindrus*. *Limnol. Oceanogr.* **54**, 1176–1196 (2009).
- 688 58. Serôdio, J. & Lavaud, J. A model for describing the light response of the nonphotochemical quenching of  
689 chlorophyll fluorescence. *Photosynth. Res.* **108**, 61–76 (2011).
- 690 59. Behrenfeld, M. J. *et al.* Revaluating ocean warming impacts on global phytoplankton. *Nat. Clim. Chang.* **6**, 323–330  
691 (2015).
- 692 60. Organelli, E. *et al.* A novel near-real-time quality-control procedure for radiometric profiles measured by bio-argo  
693 floats: Protocols and performances. *J. Atmos. Ocean. Technol.* **33**, 937–951 (2016).
- 694 61. Lacour, L., Larouche, R. & Babin, M. In situ evaluation of spaceborne CALIOP lidar measurements of the upper-  
695 ocean particle backscattering coefficient. *Opt. Express* **28**, 26989 (2020).
- 696 62. Morel, A. *et al.* Examining the consistency of products derived from various ocean color sensors in open ocean  
697 (Case 1) waters in the perspective of a multi-sensor approach. *Remote Sens. Environ.* **111**, 69–88 (2007).
- 698 63. Caputi, L. *et al.* Community-Level Responses to Iron Availability in Open Ocean Plankton Ecosystems. *Global*  
699 *Biogeochem. Cycles* **33**, 391–419 (2019).
- 700 64. Llort, J., Levy, M., Sallee, J.-B. & Tagliabue, A. Onset, intensification, and decline of phytoplankton blooms in the  
701 Southern Ocean. *ICES J. Mar. Sci.* fsv053- (2015). doi:10.1093/icesjms/fsv053

- 702 65. Uchida, T. *et al.* Southern Ocean Phytoplankton Blooms Observed by Biogeochemical Floats. *J. Geophys. Res.*  
703 *Ocean.* **124**, 7328–7343 (2019).
- 704 66. Ardyna, M. *et al.* Delineating environmental control of phytoplankton biomass and phenology in the Southern  
705 Ocean. 1–9 (2017). doi:10.1002/2016GL072428
- 706 67. Swart, S., Speich, S., Ansorge, I. J. & Lutjeharms, J. R. E. An altimetry-based gravest empirical mode south of  
707 Africa: 1. Development and validation. *J. Geophys. Res. Ocean.* **115**, (2010).
- 708